

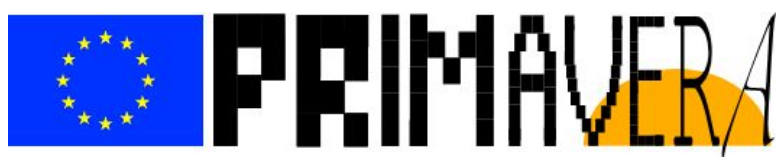


Call: H2020-SC5-2014-two-stage

Topic: SC5-01-2014

PRIMAVERA

Grant Agreement 641727



PRocess-based climate sIMulation: AdVances in high resolution modelling and European climate Risk Assessment

Deliverable D2.4

Assessment of the impact of large-scale drivers (from WP5) on processes that benefit from increased resolution across the multi-model ensemble, and their sensitivity to climate change based on the WP6 Stream 1 simulations.

Deliverable Title	<i>Assessment of the impact of large-scale drivers (from WP5) on processes that benefit from increased resolution across the multi-model ensemble, and their sensitivity to climate change based on the WP6 Stream 1 simulations.</i>	
Brief Description	<i>The deliverable focuses on how climate processes are affected by large-scale drivers such as natural modes of variability (AMV, ENSO, PDO), the AMOC and Arctic sea ice. A main goal is to assess the ability of the models in reproducing the observed teleconnections and the role of the increased resolution, analyzing either WP6 or WP5 simulations. Hence the implication for processes of future changes in the large-scale drivers are discussed.</i>	
WP number		WP2
Lead Beneficiary	CNR	
Contributors	<i>Federico Fabiano (CNR) Paolo Ghinassi (CNR) Virna Meccia (CNR) Susanna Corti (CNR) Malcolm Roberts (MetOffice) Yohan Ruprich-Robert (BSC) Ramón Fuentes-Franco (SMHI) Klaus Zimmermann (SMHI) Torben Koenigk (SMHI) Franco Molteni (ECMWF) Christopher D. Roberts (ECMWF) Retish Senan (ECMWF) Sarah P. E. Keeley (ECMWF) G. Fedele (CMCC) A. Bellucci (CMCC) S. Masina (CMCC) Svenya Chripko (CERFACS) Rym Msadek (CERFACS) Emilia Sanchez-Gomez (CERFACS) Jorge Lopez-Parages (CERFACS) Laurent Terray (CERFACS) Steve Delhayé (UCLouvain) François Massonnet (UCLouvain) Thierry Fichefet (UCLouvain) David Docquier (UCLouvain)</i>	
Creation Date		12/12/2019
Version Number		2.4

Version Date		31/01/2020
Deliverable Due Date		01/02/2020
Actual Delivery Date		31/01/2020
Nature of the Deliverable	R	<i>R - Report</i>
		<i>P - Prototype</i>
		<i>D - Demonstrator</i>
		<i>O - Other</i>
Dissemination Level/ Audience	PU	<i>PU - Public</i>
		<i>PP - Restricted to other programme participants, including the Commission services</i>
		<i>RE - Restricted to a group specified by the consortium, including the Commission services</i>
		<i>CO - Confidential, only for members of the consortium, including the Commission services</i>

Version	Date	Modified by	Comments
1	22/01/2020	Federico Fabiano, Paolo Ghinassi (CNR), WP2 partners	Original contributions included
2	29/01/2020	Federico Fabiano, Paolo Ghinassi (CNR), WP2 partners	Executive summary and Lessons learnt added; corrections from partners included
3	31/01/2020	Federico Fabiano, Paolo Ghinassi, Virna Meccia, Susanna Corti (CNR)	Final revision

Table of Contents

1. Executive Summary	6
2. Project Objectives	8
3. Detailed Report	9
3.1 Atlantic Multidecadal Variability (AMV)	10
3.1.1 Climate impacts of the observed AMV	10
3.1.2 Impact of AMV on Atlantic SST in HR and LR	14
3.1.3 Impact of AMV on the occurrence of North-Atlantic Weather Regimes	15
3.2 El Niño Southern Oscillation (ENSO)	19
3.2.1 ENSO spectrum and impact of ENSO and PNA on precipitation	19
3.2.2 Boreal-winter teleconnections with ENSO and Western/Central Indian Ocean (WCIO) precipitation	21
3.2.3 ENSO influence on Tropical North Atlantic SSTs	26
3.2.4 ENSO impact on the Pacific-North American weather regimes	27
3.3 Sea Ice	32
3.3.1 Impact of Arctic sea ice decline on the NH mid-latitudes climate	32
3.3.2 Impact of horizontal resolution on the climatic responses due to Arctic sea ice loss	33
3.4 Atlantic Meridional Overturning Circulation (AMOC)	38
3.4.1 Influence of Atlantic Meridional Overturning Circulation on Northern Hemisphere temperatures	38
3.5 Pacific Decadal Oscillation (PDO)	40
3.5.1 The influence of the PDO on the Kuroshio Extension low-frequency variability	40
4. Lessons Learnt	47
4.1 Assessment of the model performance in reproducing the observed teleconnections	47
4.2 Impact of the increased resolution on teleconnections	47
4.3 Potential implications for the future	48
5. Links Built	49

1. Executive Summary

The deliverable focuses on how climate processes are affected by large-scale drivers such as natural modes of climate variability (Atlantic Multidecadal Variability, AMV; El Niño - Southern Oscillation, ENSO; Pacific Decadal Oscillation, PDO), the Atlantic Meridional Overturning Circulation (AMOC) and the Arctic sea ice. The main goal is to assess the ability of the PRIMAVERA models in reproducing the observed teleconnections between drivers and processes and to determine the effect of the increased resolution on the model performance. A wide variety of drivers and processes has been considered, reflecting the specific research interests of each group participating in the project. Hence, it is difficult to draw a general picture of the model performance or the impact of increased resolution, that are strongly dependent on the drivers and processes analyzed. Also, conclusions may vary across the multi-model ensemble, depending on model-dependent biases.

Nevertheless, the models manage to reproduce correctly several observed teleconnection mechanisms, although generally with a large variability in the amplitude of the response across the multi-model ensemble. This is the case for the teleconnection of the AMV with the tropical/North Pacific ocean SSTs (3.1.1), which models are able to reproduce but with significantly different amplitudes. It is worth noting that the amplitude of the response correlates well with inter-model differences in the intertropical Atlantic surface temperature gradient. Most of the models are able to get the right direction of the AMV impact on the frequency of occurrence of wintertime Euro-Atlantic Weather Regimes (3.1.2), although they tend to underestimate the amplitude of the response with respect to the observations.

Regarding the drivers in the Pacific region, the model performance is generally good in capturing the dominant frequencies of the ENSO energy spectrum (3.2.1), but the amplitude of the power spectrum varies largely among the models. ENSO is the main driver of several teleconnection mechanisms, which are in general fairly represented in the PRIMAVERA models. Examples of this are the impact of ENSO-related precipitation on the boreal mid-latitude circulation in late winter (3.2.2) and the teleconnection of ENSO with Tropical North Atlantic (TNA) SSTs (3.2.3). Also, the effect of ENSO on the wintertime Pacific-North American (PNA) Weather Regimes is generally caught by models (3.2.4), although there is a large variability across the multi-model ensemble and a common tendency to underestimate this effect. Moving to the Northern Pacific, the teleconnection between the PDO and the low-frequency variability of the Kuroshio Extension (KE) is reported to be well represented in the CMCC model (3.5.1).

There are also some cases in which the models are not able to reproduce the observed teleconnection. An example of this is the effect of the AMV on average European surface temperature and geopotential (3.1.1), that is represented by models not only with varying amplitudes, but also with opposite signs. Also, reported to be much weaker in models or missing at all are the teleconnection of the Western/Central Indian Ocean precipitation with the boreal winter circulation (3.2.2) and the link of the Pacific Trough regime with ENSO SSTs and with the North-Atlantic geopotential (3.2.4).

For most of the teleconnections mentioned above, no clear impact of the increased horizontal resolution on the model performance has been detected (3.1.1, 3.1.3, 3.2.2, 3.2.4,

3.5.1). Nevertheless, the increased resolution is reported to impact some specific teleconnections. A good example of the latter case is the ENSO-TNA link, which is better reproduced in the HR multi-model ensemble, due to a better representation of the Atlantic state (3.2.3). Another example is the correlation of the AMOC with the mean surface air temperature in the HadGEM model, which switches from positive to negative in the subpolar gyre (mainly over Greenland and parts of North-America) with increasing ocean resolution (3.4.1).

The increase of both atmospheric and oceanic resolutions is found to produce an enhanced ENSO SST pattern (3.2.1), though this is not producing a net effect on the related precipitation. Increased atmospheric resolution also tends to induce an enhanced AMV pattern, with warmer SSTs and larger associated precipitation anomalies (3.1.2). In other respects, the effect of increasing either the atmospheric or the oceanic resolutions goes in opposite directions. In particular, ocean HR tends to increase the amplitude of the ENSO power spectrum, while the atmospheric HR tends to decrease it (3.2.1).

The sea ice loss response to the albedo reduction in WP5 sensitivity experiments is both model dependent (CNRM-CM6 and ECMWF-IFS) and resolution dependent (ECMWF-IFS) (3.3.1, 3.3.2). The impact of the increased atmospheric resolution on the sea-ice teleconnections appears to be model dependent as well. A consistent atmospheric response is found in the HR and LR versions of the CNRM model (3.3.1), while the ECMWF HR and LR models show different responses in terms of surface pressure, due to different patterns of sea ice loss (3.3.2). However, despite these differences, a weakening of the stratospheric polar vortex is detected in response to the sea ice loss in both models, with the increased resolution producing a stronger change (3.3.1, 3.3.2).

2. Project Objectives

With this deliverable, the project has contributed to the achievement of the following objectives (DOA, Part B Section 1.1) WP numbers are in brackets:

No.	Objective	Yes	No
A	To develop a new generation of global high-resolution climate models. (3, 4, 6)		x
B	To develop new strategies and tools for evaluating global high-resolution climate models at a process level, and for quantifying the uncertainties in the predictions of regional climate. (1, 2, 5, 9, 10)	✓	
C	To provide new high-resolution protocols and flagship simulations for the World Climate Research Programme (WCRP)'s Coupled Model Intercomparison Project (CMIP6) project, to inform the Intergovernmental Panel on Climate Change (IPCC) assessments and in support of emerging Climate Services. (4, 6, 9)		x
D	To explore the scientific and technological frontiers of capability in global climate modelling to provide guidance for the development of future generations of prediction systems, global climate and Earth System models (informing post-CMIP6 and beyond). (3, 4)		x
E	To advance understanding of past and future, natural and anthropogenic, drivers of variability and changes in European climate, including high impact events, by exploiting new capabilities in high-resolution global climate modelling. (1, 2, 5)	✓	
F	To produce new, more robust and trustworthy projections of European climate for the next few decades based on improved global models and advances in process understanding. (2, 3, 5, 6, 10)	✓	
G	To engage with targeted end-user groups in key European economic sectors to strengthen their competitiveness, growth, resilience and ability by exploiting new scientific progress. (10, 11)		x
H	To establish cooperation between science and policy actions at European and international level, to support the development of effective climate change policies, optimize public decision making and increase capability to manage climate risks. (5, 8, 10)		x

3. Detailed Report

The main goal of this deliverable is to evaluate the model performance in representing observed teleconnections between large-scale drivers and climate processes and to assess the impact of the increased resolution on these teleconnections. The different contributions focus on a wide variety of drivers and processes, reflecting the peculiar research interests of each group participating to the project. The structure of the deliverable reflects the different large-scale drivers under study: the Atlantic Multidecadal Variability (AMV, Section 3.1), the El Niño – Southern Oscillation (ENSO, Section 3.2), the Arctic sea-ice (Section 3.3), the Atlantic Meridional Overturning Circulation (AMOC, Section 3.4) and the Pacific Decadal Oscillation (PDO, Section 3.5). Some contributions inside the ENSO section (3.2) also focus on different drivers/modes of variability such has the Western/Central Indian Ocean (WCIO) precipitation (3.2.2), the Pacific-North American pattern (3.2.1) and the Pacific Trough weather regime (3.2.4). Nevertheless we decided to keep them inside Section 3.2 since ENSO is closely connected to the mechanisms studied.

A large set of simulations was available both from WP5 and WP6, and different experiments have been used for the analyses contained in this deliverable, as shown in Table 3.0.1. The hist-1950, control-1950 and highresSST-present experiments have already been thoroughly described in deliverable D2.2. The WP5 experiments analyzed follow two different protocols: 1) a set of AMV sensitivity runs with imposed SSTs in the North Atlantic corresponding to the positive and negative phases of AMV (more details in Section 3.1.1); 2) a set of sea-ice sensitivity simulations in which the sea-ice albedo parameter has been set to the ocean value, in order to reduce the sea ice extent (more details in Sections 3.3.1 and 3.3.2). More results about the WP5 AMV sensitivity runs are reported in the dedicated D5.2 deliverable *“Report documenting the impacts of AMV and IPV, and changes in direct radiative forcing, on the European climate of the most recent period and sensitivity to resolution and physics choices”*.

Experiments	Deliverable sections
hist-1950	3.1.2, 3.1.3, 3.2.1, 3.2.2, 3.2.4
control-1950	3.2.3, 3.4.1, 3.5.1
highresSST-present	3.2.2
WP5 (AMV, sea-ice)	3.1.1, 3.3.1, 3.3.2

Table 3.0.1 Experiments analyzed in the different sections of the deliverable.

3.1 Atlantic Multidecadal Variability (AMV)

During the last century, the North Atlantic SST exhibited a long-term warming trend with superimposed multidecadal fluctuations. This multidecadal variability is referred to as the Atlantic Multidecadal Variability (AMV). The AMV is thought to be at the origin of marked climate anomalies with substantial impacts upon human activities over many areas of the globe. These include droughts over Africa (in particular the extremely severe 70s-80s Sahelian drought, responsible for 100,000 fatalities; UN report 2002) and North America, decline in Arctic sea ice, changes in tropical cyclone activity, and the recent global temperature hiatus (Mohino et al. 2011; Enfield et al. 2001; Mahajan et al. 2011; Vimont and Kossin 2007; McGregor et al. 2014; Li et al. 2015). The North Atlantic SST is also a main driver of European climate variability. Previous studies proposed a causal link between the warm phase of the AMV and warm conditions over Central Europe, dry conditions over the Mediterranean basin, and wet conditions over Northern Europe (Sutton and Hodson 2005; Sutton and Dong 2012), modulating the river streamflow and electricity production (Boé and Habets 2014). The AMV can also impact the location and activity of the North Atlantic extratropical storms by modulating the large scale atmospheric circulation (Hakkinen et al. 2011; Peings and Magnusdottir 2014; Gastineau and Frankignoul 2012). Given the numerous climate impacts of the AMV and their related consequences on human society, understanding its teleconnections in order to better predict them is of high interest.

3.1.1 Climate impacts of the observed AMV (BSC)

To isolate the impacts of the observed AMV on climate, we performed in Primavera WP5 coordinated idealized numerical simulations with 9 different Coupled Global Climate Models (CGCMs): CNRM-CM6-LR, EC-Earth3P, EC-Earth3P-HR, ECMWF-IFS-LR, ECMWF-IFS-HR, MPI-ESM1-2-HR, MPI-SM1-2-XR, MetUM-GOML2-LR and MetUM-GOML2-HR. Following the DCPP-C protocol (Boer et al. 2016), two sets of ensemble simulations have been performed with each model, in which time-invariant SST anomalies corresponding to the warm (AMV+) and cold (AMV-) phases of the observed AMV were imposed over the North Atlantic. To focus on the internal climate response and to capture the potential response and adjustment of other oceanic basins to the AMV anomalies, the simulations were integrated for 10 years with fixed external forcing conditions. Ensemble simulations were performed in order to robustly estimate the climate impacts of AMV (from 10 to 32 members depending on the model). An extensive description of the experimental protocol is provided by the Technical note for AMV DCPP-C simulations: <https://www.wcrp-climate.org/wgsip/documents/Tech-Note-1.pdf>. We stress that our simulations deviate from the exact AMV DCPP-C protocol. To increase the signal-to-noise ratio of the AMV impacts, the imposed AMV anomalies have been multiplied by 2 with respect to the DCPP-C protocol. In addition:

- CNRM-CM6-LR, EC-Earth3P-LR, EC-Earth3P-HR, ECMWF-IFS-HR, ECMWF-IFS-LR, MPI-ESM1-2-HR and MPI-ESM1-2-XR used a constant 1950 (instead of 1850) external forcing background,

- MetUM-GOML2-HR and MetUM-GOML2-LR simulations used a 2000 external forcing background and an ocean mixed-layer model of 1000 m depth on 100 vertical levels instead of a fully dynamical ocean.

We focus here on the AMV impacts in terms of 2-meter air temperature (T_{2m}) and geopotential height 500hPa (ZG500) during the boreal winter season defined here as December to March (DJFM). In addition, we only discuss the difference between the 10-year ensemble mean average of the AMV+ and AMV- experiments.

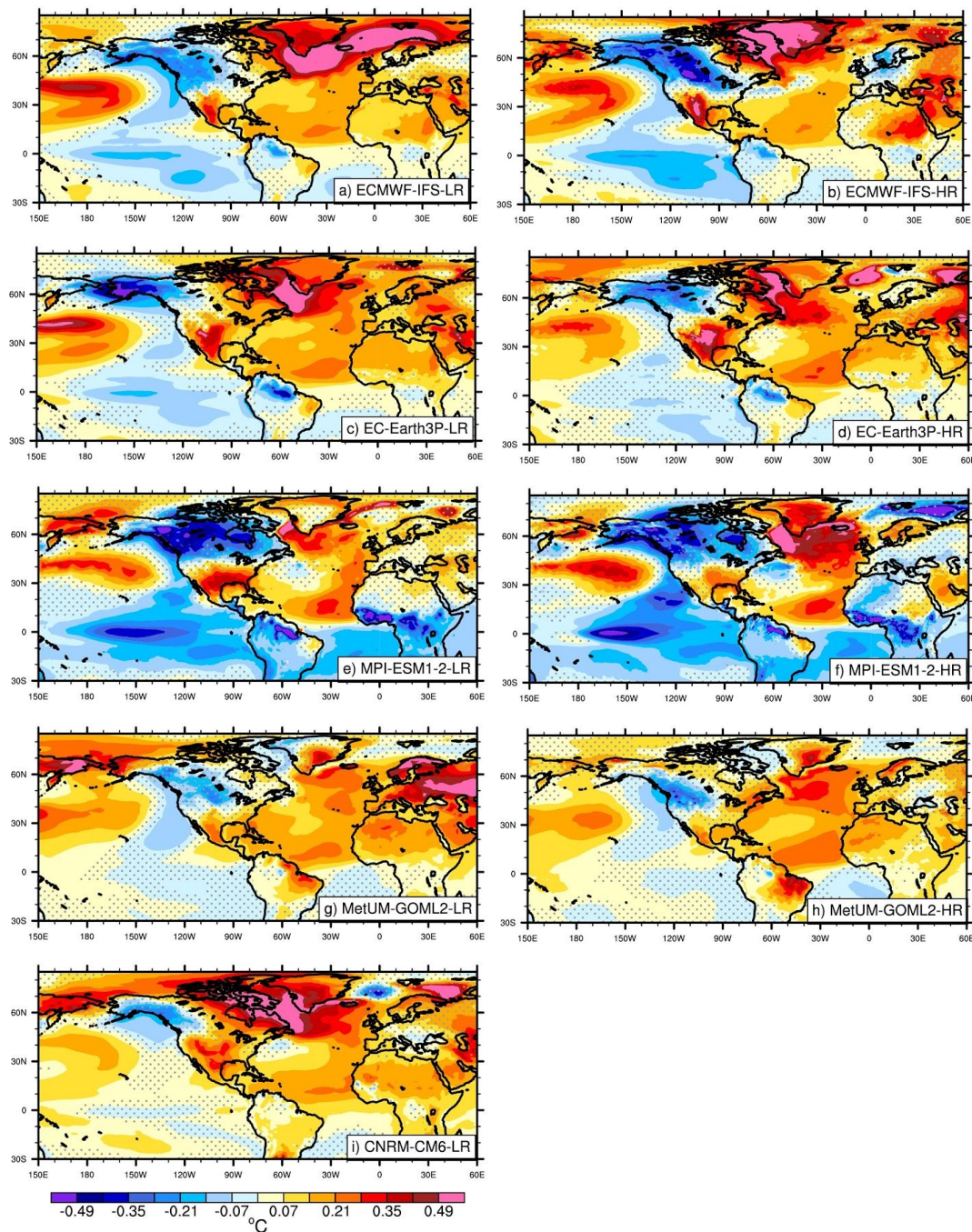


Figure 3.1.1.1 December-January-February-March 2-meter air temperature difference between the 10-year ensemble mean average of the AMV+ and AMV- experiments. Stippling

indicates regions that are below the 95% confidence level of statistical significance according to a two-sided t-test.

a) Pacific ocean response

In response to an observed AMV warming, models tend to simulate a tropical Pacific cooling that extends to the North Pacific through the East (Figure 3.1.1.1). This cooling contrasts with warm anomalies over the Pacific Northwest. The amplitude of those anomalies is model dependent. In particular, there is a factor 10 in the amplitude of the NINO3.4 SST index cooling between the response simulated by MPI-ESM1-2-HR and CNRM-CM6-LR. The reasons behind the AMV-tropical Pacific teleconnection and its inter-model spread are the subject of an article in preparation (Ruprich-Robert et al. in prep.).

The mechanism proposed is that warmer tropical Atlantic initiates changes in the Atlantic-Pacific Walker circulation in boreal summer, which modifies the western tropical Pacific surface winds. The Indo-Pacific Walker circulation accelerates in response to this surface wind changes. It acts as a positive feedback on the initial tropical Pacific response to the Atlantic forcing. All together, the Walker circulation changes eventually leads to the development of a tropical Pacific cooling in boreal winter. We found that the inter-model spread is mostly coming from the Indo-Pacific Walker circulation feedback and the strength of the associated atmospheric convection over the Warm Pool. The latter is tightly linked to the Warm Pool warming response relatively to the upper tropospheric temperature of the whole tropical belt, which its inter-model spread appears to be controlled by the cooling response in the South Atlantic. Therefore, we conclude that, un-intuitively, the La Niña-like response to an AMV warming is ultimately constrained by the strength of the intertropical Atlantic surface temperature gradient. Finally, we tracked back the origin of the inter-model spread of this intertropical Atlantic temperature gradient and we found that it is coming from the different representation of SST-low cloud relationship among the models. The models simulating the strongest relationship are the models simulating the strongest La Niña-like anomalies in response to an AMV warming.

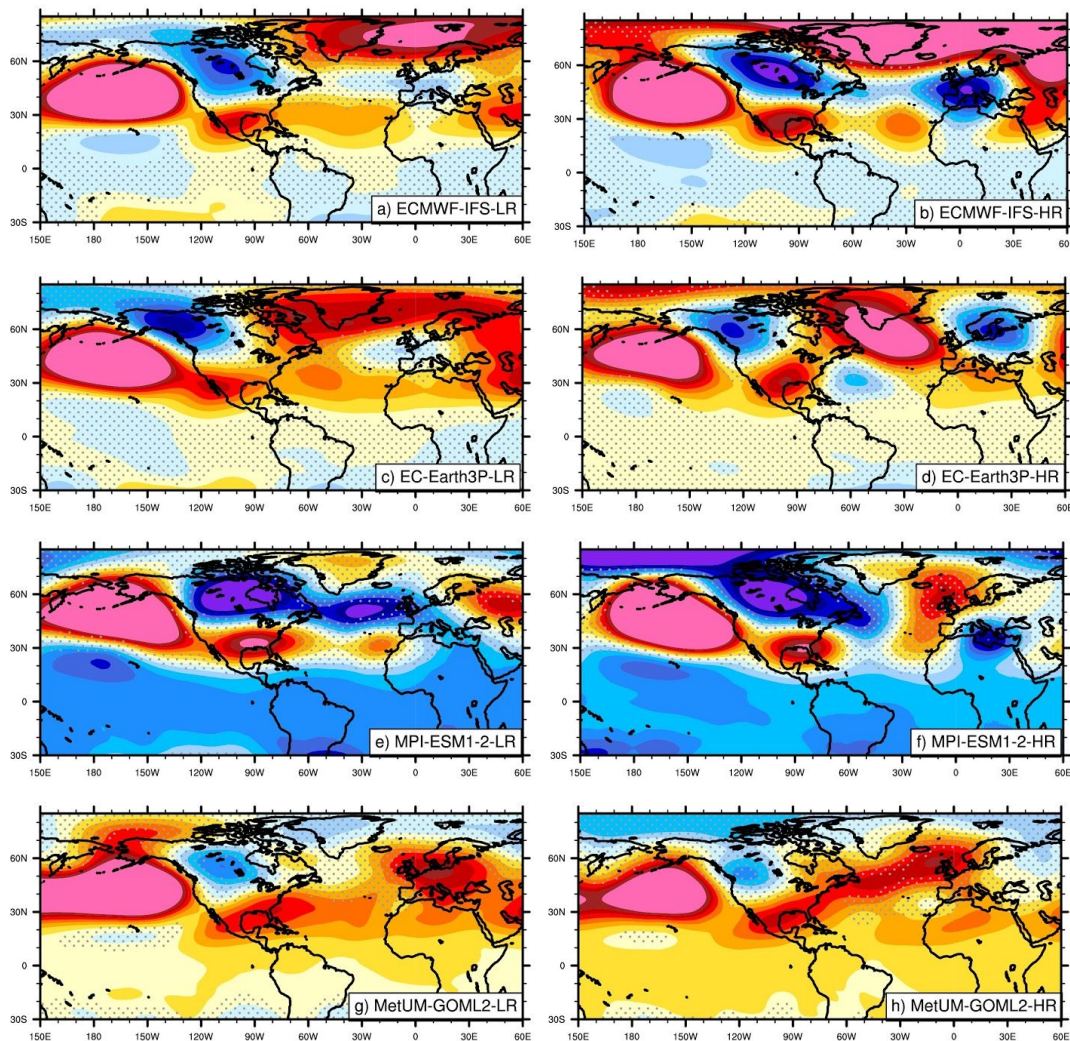
b) Continental response

In addition to the Pacific response, models simulate a warming over the south of North America and a cooling over the north-west of North America (Figure 3.1.1.1). Yet, the amplitude of the exact extension of this cooling is model dependent. For the 2 MPI-ESM1-2 models, the cooling extends over the entire Canada whereas for the EC-Earth3P-LR model the cooling is mostly confined to Alaska. Over the northern part of Africa, all the models except the 2 MPI-ESM1-2 models simulate a warming.

There is a large inter-model spread response over Europe, especially over the north-west where some models simulate a cooling and other simulate a warming. A large inter-model spread is also found in the ZG500 response to AMV over the North Atlantic - Europe region (Figure 3.1.1.2). The different atmospheric response among the models could therefore explain the differences in T2m response as argued in Qasmi et al. (2020). In particular, in the absence of an atmospheric circulation response to an AMV warming, one would expect the presence of positive T2m anomalies over western Europe through the advection by the mean flow of warm anomalies from the North Atlantic. Following this perspective, the

cyclonic anomalies over Europe simulated in the ECMWF-IFS-HR and MPI-ESM1-2-HR models could explain the absence of positive anomalies over western Europe. The study of the inter-model spread response to a warming in terms of North Atlantic - Europe atmospheric circulation is the object of an article led by Ruggieri et al. (submitted). In this study, we argue that in response to an AMV warming, the Atlantic storm track is contracted and less extended poleward and the low-level jet is shifted towards the equator in the Eastern Atlantic. We demonstrate a link between model bias and features of the jet response.

Over the Pacific - North America sector, all models simulate a Pacific North America (PNA) pattern response in its negative phase, with a decrease of the Aleutian low. Yet, the exact locations of the centers of action of the PNA response vary among models. This may also explain the difference of the temperature anomalies over North America. In particular, the models simulating cyclonic anomalies over the whole Canada also simulate cold anomalies all over Canada (e.g., MPI and ECMWF models).



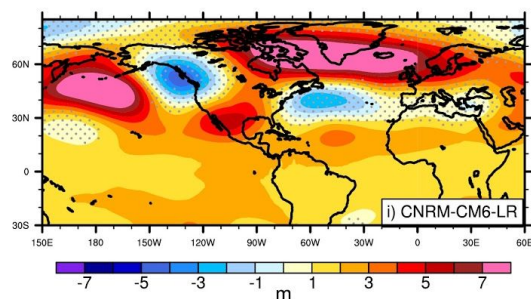


Figure 3.1.1.2 As Figure 3.1.1.1 but for ZG500.

3.1.2 Impact of AMV on Atlantic SST in HR and LR (SMHI)

The climate variability diagnostics toolbox (CVDP) was used to calculate the AMV and other variability modes (see Section 3.2.1) over the following simulations and ensemble members: ECMWF-IFS-LR (8 members), ECMWF-IFS-MR (3 members), ECMWF-IFS-HR (6 members), CMCC-CM2-HR4, CMCC-CM2-VHR4, MPI-ESM1-2-HR, MPI-ESM1-2-XR, HadGEM3-GC31-LL (8 ensemble members), HadGEM3-GC31-MM, HadGEM3-GC31-HM, HadGEM3-GC31-HH. For the models that had more than one ensemble member, the modes were calculated separately and their respective ensemble average was calculated. The period considered was 1950-2014 for all models and 1979-2018 for observations (ERA Interim, GPCP).

With increased atmospheric resolution, the AMV shows slightly warmer SST over regions of the North Atlantic, showing its maximum over the Barents sea. Associated with this change it is found more precipitation over the regions showing warmer SST conditions. However, the increase in ocean resolution show diverging results in the SST and its precipitation associated.

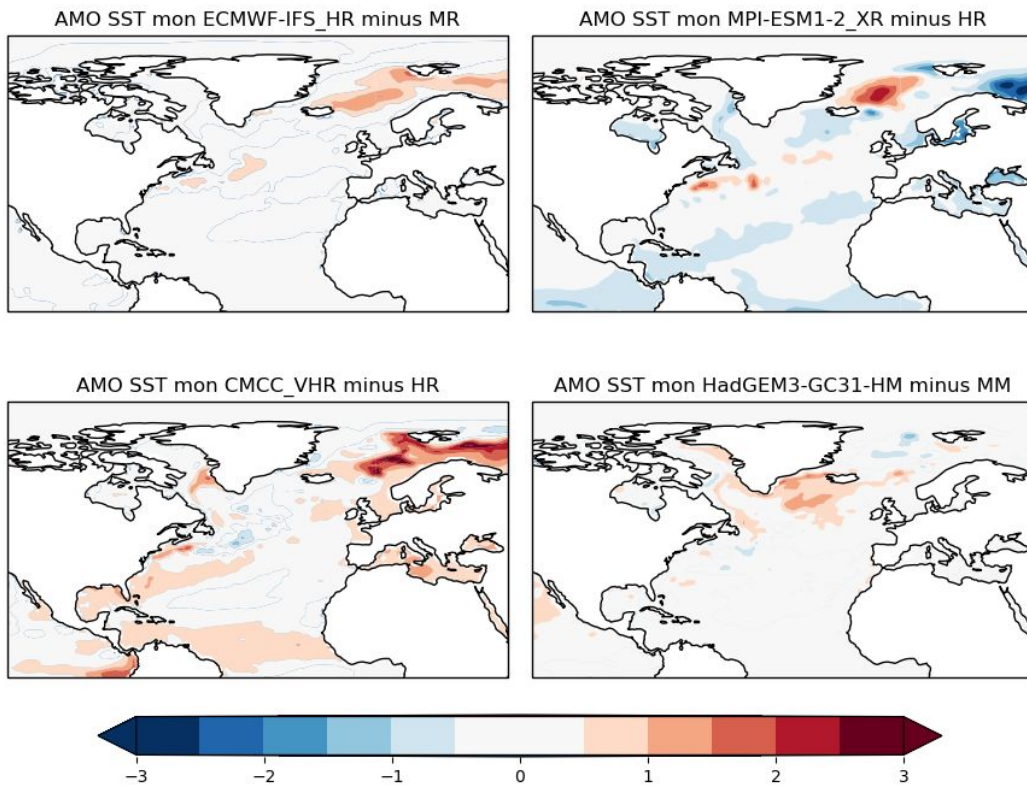


Figure 3.1.2.1 SST difference between high and coarse atmospheric model resolutions for ECMWF-IFS (upper left), MPI-ESM1-2 (upper right), CMCC-CM2 (lower left) and HadGEM3-GC31 (lower right). Colorbar units are Kelvin.

3.1.3 Impact of AMV on the occurrence of North-Atlantic Weather Regimes (CNR)

Weather Regimes (WRs) are persistent dynamical configurations that can last from a few days to two or three weeks (synoptic scale) (Straus et al., 2007; Dawson et al., 2012; Hannachi et al., 2017). Here we analyze the link of the wintertime WRs with the large-scale modes of variability of the climate system, both in the reanalysis and in the hist-1950 PRIMAVERA simulations. At first we focus on the influence of the Atlantic Multidecadal Variability (AMV) on the Euro-Atlantic (EAT) WRs. Then, in Section 3.2.4 we investigate the impact of ENSO on the Pacific-North American (PNA) WRs.

The WRs are calculated on the daily 500 hPa geopotential height anomalies. An Empirical Orthogonal Function (EOF) decomposition is applied, restricting the analysis to the first 4 Principal Components (PCs). Weather Regimes are identified by applying a k-means clustering algorithm to the PCs. We considered 4 clusters both for the EAT and PNA sectors.

The WRs were computed for all models/members of the PRIMAVERA hist-1950 ensemble, considering the DJFM season and the period 1957-2014. For the EAT region the following regimes have been identified:: NAO+, Scandinavian Blocking (SBL), NAO- and Atlantic Ridge (AR). We computed the AMV index for all models/ensemble members of the hist-1950 runs. To construct the index, the globally area-averaged (180°W - 180°E and 60°S - 60°N) SST anomalies was subtracted to the North Atlantic area-averaged (80°W - 0°W and 0° - 60°N) SST anomalies (Trenberth et al., 2019b). Then, a 5-year running mean was applied to the annual means of the calculated index.

Positive vs negative AMV

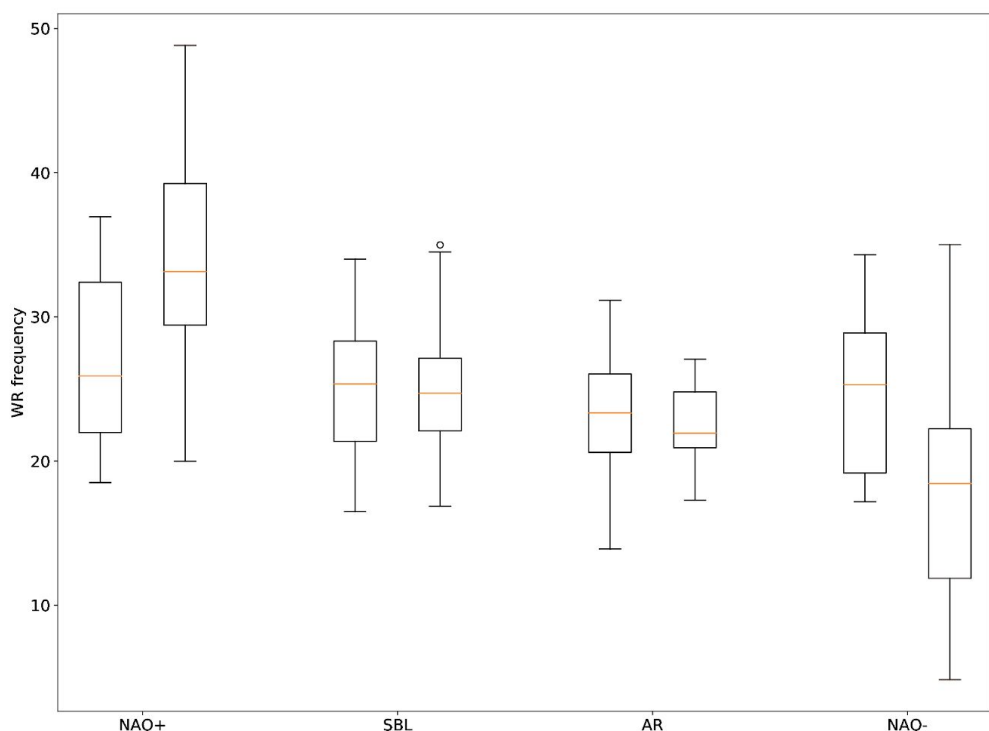


Figure 3.1.3.1 Frequency of occurrence of the EAT regimes with positive (left bar) and negative (right bar) phases of the AMV for the ERA (40 + Interim) reanalysis (1957-2014). A 5 year running mean has been applied both to the AMV index and to the WR frequencies.

Previous works identified a significant anti-correlation of the AMV with the NAO index in observations, with positive phases of AMV leading to negative NAO and increased atmospheric blocking (Hakkinen et al., 2011). This connection also holds in a WRs perspective, with an increased occurrence of the NAO- (NAO+) regime during periods of positive (negative) AMV (Peings and Magnusdottir, 2014). The link was found to be stronger in late winter (FM).

Figure 3.1.3.1 shows the frequency of the different regimes for the ERA (40 + Interim) reanalysis, under the two phases of the AMV. The effect on the NAO+ and NAO- regimes is

clear, with no significant change for the other two regimes. This is reflected in the correlation of the AMV index with the seasonal frequency of occurrence of the regimes: the correlation of the NAO- (NAO+) regime frequency with the AMV is about 0.47 (-0.40).

WR freq. difference between positive and negative phase of AMV - DJFM

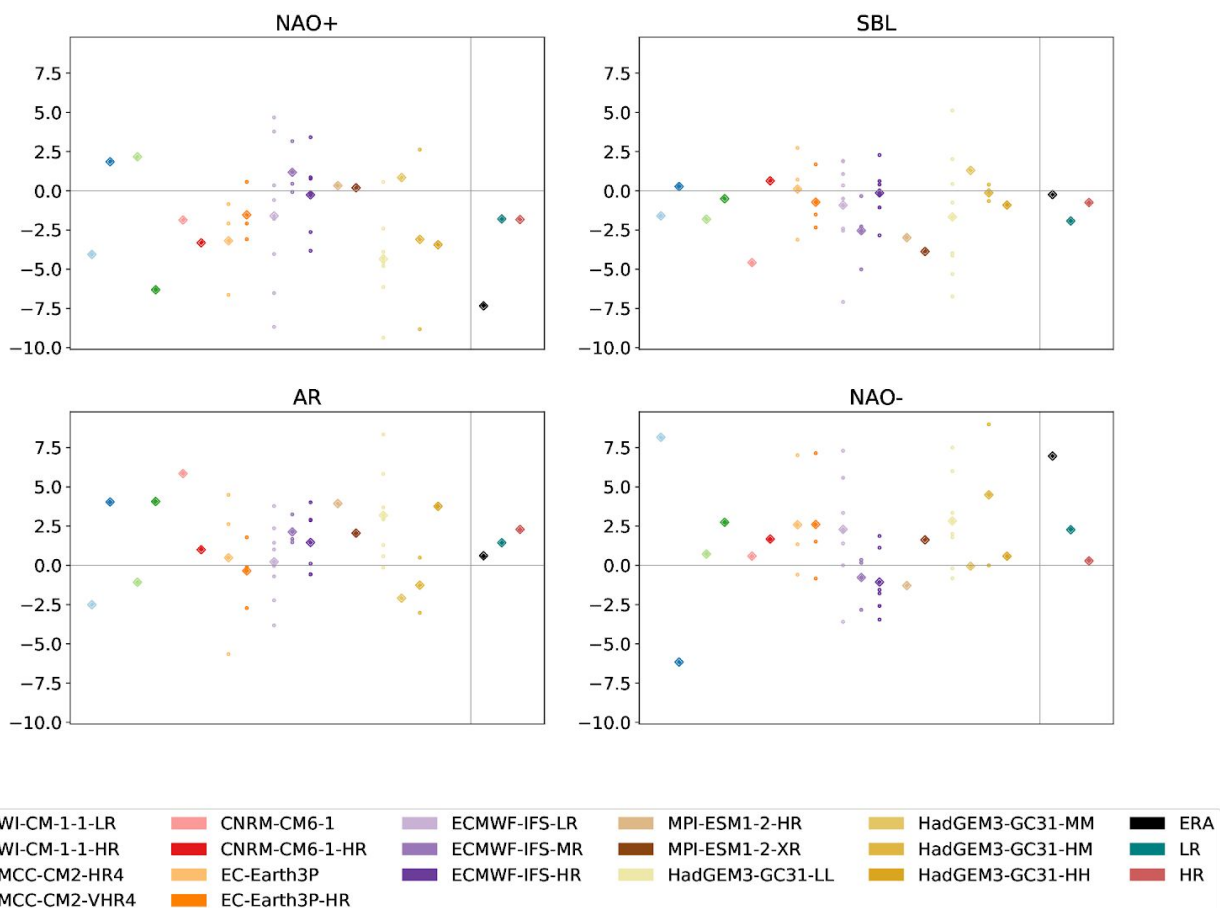


Figure 3.1.3.2 Difference in the seasonal regime frequency between AMV+ and AMV- seasons for all models/members in the hist-1950 ensemble. The diamonds show the model average, the dots the individual members. To the right of the vertical line, the observed value and the average of all lowest (LR) and highest (HR) model versions are shown.

Then, we analyzed how the relation between EAT regimes and AMV is reproduced in the models. Figure 5 shows the difference in frequency of each WR distinguishing between AMV+ and AMV- seasons for all models in the hist-1950 ensemble. For each model, before computing the correlation, a 5 year running mean has been applied both to the AMV index and to the seasonal regime frequencies.

The response in models tends to be in the right direction for the two NAO regimes, but a considerable variability can be noticed, with a large inter-member spread and some models that go in the wrong direction. Also, the response in the models tends to be of smaller amplitude. The increased resolution does not affect these results in a clear and systematic way. The large variability and the poor performance of some models/members in capturing

the correlation may be partly caused by the short period considered, further analysis on the control-1950 and WP5 sensitivity runs is needed to better assess the model performance.

3.2 El Niño Southern Oscillation (ENSO)

El Niño – Southern Oscillation (ENSO) is one of the strongest modes of variability of the climate system. The positive phase of ENSO is characterized by anomalous high SSTs over the eastern tropical Pacific, with reduced easterly winds and enhanced convection in the region. The negative phase sees instead an anomalous cooling of the region. The ENSO has an irregular period - with most of the power between 2 and 5 years - and varying intensity, with each episode lasting several months. ENSO strongly affects the climate of the tropics (Scaife et al., 2017), subtropics and extratropics through teleconnections (Shaman, 2014; Schemm, 2018). During winter, El Niño tends to cause increased precipitation over California, Southern USA and Northern Mexico, and drier conditions over Southwestern Canada, and Northwestern USA. In turn, La Niña increases the chances of dry conditions over Southern USA and wetter conditions the Northwest USA and Western Canadian coast.

3.2.1 ENSO spectrum and impact of ENSO and PNA on precipitation (SMHI)

With increased atmospheric resolution, we find across models weaker precipitation anomalies associated with ENSO over North America than with coarser atmospheric resolution, this despite the non-systematic change on SST to atmospheric resolution across models (with ECMWF-IFS and MPI-ESM1-2 showing colder SST, while CMCC and HadGEM3-GC31 show warmer SST over the eastern and Central Pacific).

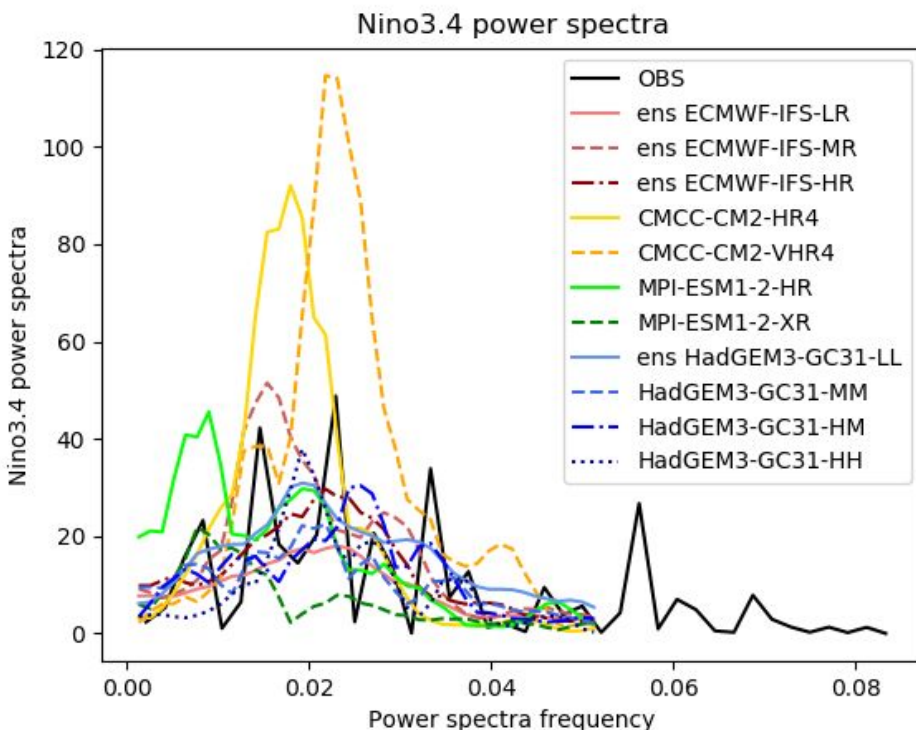


Figure 3.2.1.1 Power spectrum of Niño3.4 for the observations (ERA-Interim reanalysis), and stream 1 historical PRIMAVERA simulations. [X axis: month⁻¹, Y axis: Celsius²/cycle month⁻¹]

Increased ocean resolution also gives diverging results in ECMWF-IFS and HadGEM3-GC31 in terms of SST and precipitation, with ECMWF-IFS showing warmer SST and stronger precipitation response with higher resolution, and HadGEM3-GC31 showing the opposite.

An increase of both atmospheric and ocean resolution shows systematically across models warmer SST conditions over the eastern tropical Pacific coasts, and cooler western Pacific SSTs, compared to coarser resolutions. However, the precipitation associated with ENSO, does not show a systematic response across models increasing both ocean and atmospheric resolutions. In terms of frequency and intensity, ENSO3.4 index shows the most energetic frequencies as those of 0.022 and 0.016 months⁻¹ (approx. 3.8 and 5.2 years respectively) (see Figure 3.2.1.1). The most energetic frequencies across models are within these two maximum observed frequencies (except MPI-ESM1-2). There are no preferred frequencies with increased ocean or atmospheric model resolution, however there is a tendency to increase the energy [Celsius²/cycle month⁻¹] with an increase in the ocean resolution, and to decrease the energy with an increase in atmospheric resolution.

Consistently with the results found for precipitation associated with ENSO, the precipitation response associated with the PNA is weaker with increased atmospheric resolution, showing drier conditions over California, and south-eastern United States, and wetter conditions over the Pacific coast of Canada and Midwest US.

Increased ocean resolution results in a systematic enhanced response of PNA associated precipitation.

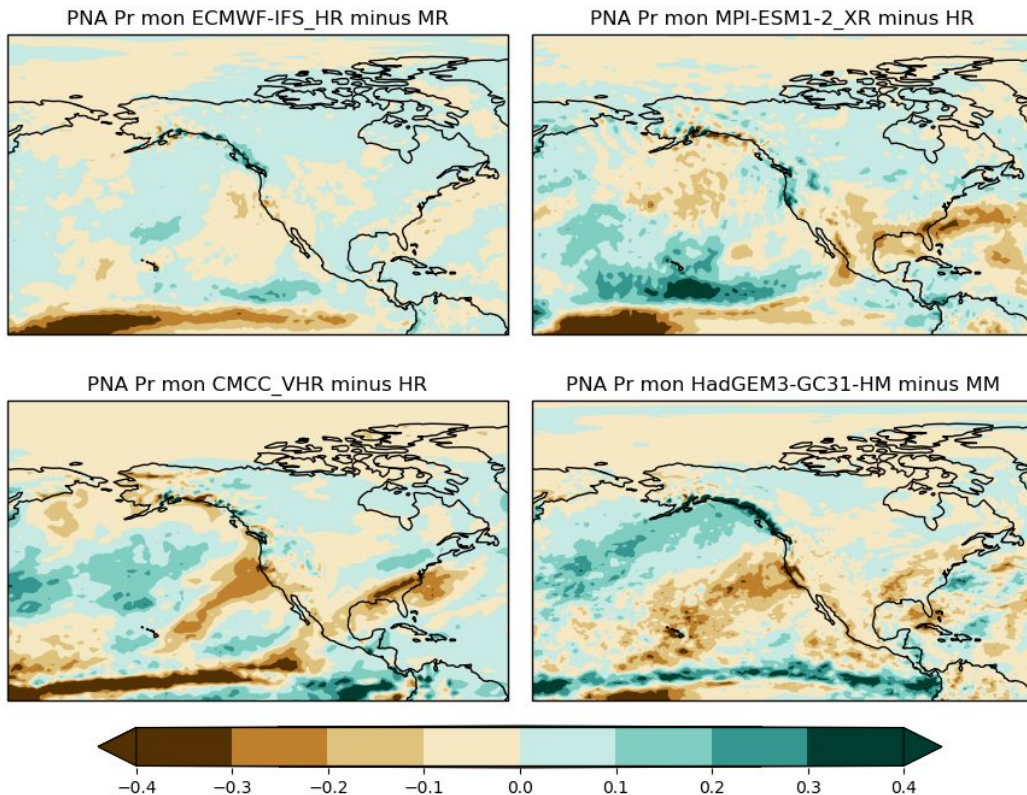


Figure 3.2.1.2 Difference of PNA's regressed precipitation between high and coarse atmospheric model resolutions for ECMWF-IFS (upper left), MPI-ESM1-2 (upper right), CMCC-CM2 (lower left) and HadGEM3-GC31 (lower right). Colorbar units are mm day^{-1} .

We found a weaker PNA response with increased atmospheric resolution, and enhanced PNA response, with increased ocean model resolution.

3.2.2 Boreal-winter teleconnections with ENSO and Western/Central Indian Ocean (WCIO) precipitation (ECMWF)

We have investigated how teleconnections linking tropical rainfall anomalies and wintertime circulation in the northern extra-tropics are represented in historical simulations for the period 1950-2010 run by six PRIMAVERA partners (CMCC, CERFACS, EC-Earth, ECMWF, MetOffice, MPI). The analysis has focussed on teleconnections from the western/central Indian Ocean (WCIO) in mid-winter and from the NINO4 region in both the early and the late part of winter; this choice is justified by a substantial change in the relationship between ENSO and the NAO in the two parts of the season (see Fig. 3.2.2.1). Model results for both

coupled integrations and runs with prescribed sea-surface temperature (SST) were validated against data from the latest ECMWF 20th-century re-analysis, CERA20C (Laloyaux et al. 2018).

Using only a single historical simulation from each model configuration, it is very difficult to detect a consistent change in the fidelity of model-generated teleconnections when either atmospheric resolution is increased or ocean coupling at high resolution is introduced. However, when simulations from six different models are pooled together in a multi-model ensemble (MME), some improvements in teleconnection patterns can be seen when moving from uncoupled to coupled simulations (see Fig. 3.2.2.2)

Comparing Fig. 2 with the left column of Fig. 3.2.2.1, it appears that agreement with observations is improved in the coupled simulation of the Indian Ocean response, which shows a wavenumber-2 pattern resembling the structure of the observed response. In the AMIP-low-res MME, the Indian Ocean teleconnection shows the strongest positive NAO signal, but its hemispheric pattern is too zonally symmetric. Both coupled and uncoupled runs do a good job in simulating the late-winter response to NINO4 rainfall. Here, coupling reduces the strength of the North Pacific response, but it increases the agreement with observations over Europe. On the other hand, in all three MMEs the early-winter response to NINO4 rainfall looks like a weaker version of the late-winter response, with only a marginal sign of a positive NAO component. In this case, the high-res AMIP ensemble shows the smallest error over the Atlantic.

For the ECMWF ensemble, on the other hand, improvements in coupled simulations can only be found for the “traditional” late-winter teleconnection from central Pacific rainfall (not shown). In particular, the teleconnection from Indian Ocean rainfall is degraded when going from uncoupled to coupled runs. The good performance of the ECMWF low resolution AMIP may be explained by the fact that the Tco199 IFS used for these runs actually has a grid resolution \approx 50-km, and in this respect is comparable to some of the models in the “high-resolution” category.

A relatively consistent signal across models is the difference in performance when teleconnections from different tropical regions and in different months are considered. While, according to a bootstrap re-sampling of CERA20C data, both the Indian Ocean teleconnection in DJ and the NINO4 teleconnection in JF are equally robust, the latter is well simulated in the majority of both uncoupled and coupled runs, while the former is reproduced with (generally) much larger errors, and a high degree of variability between individual models and ensemble members (see Fig. 3.2.2.3). Deficiencies in the Indian Ocean teleconnection may have a significant impact on the simulation of decadal variability and climate change over Europe during the cold season, when links between tropical and extratropical variability are of major importance.

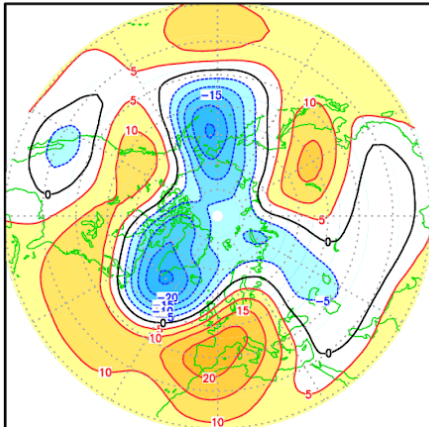
A good fidelity in simulating teleconnections on an inter-annual time scale is not necessarily reflected in a realistic estimate of multi-decadal changes between the first and the second part of the 60-year record covered by the historical runs. For AMIP runs, this is mainly due to their inability to simulate an Indian Ocean rainfall change which, in observations, has an opposite zonal gradient with respect to SST changes. In coupled runs, at least one model

run with both realistic teleconnections and a good simulation (for whatever cause) of the inter-decadal pattern of Indian Ocean rainfall also shows a realistic NAO signal in extratropical multi-decadal variability.

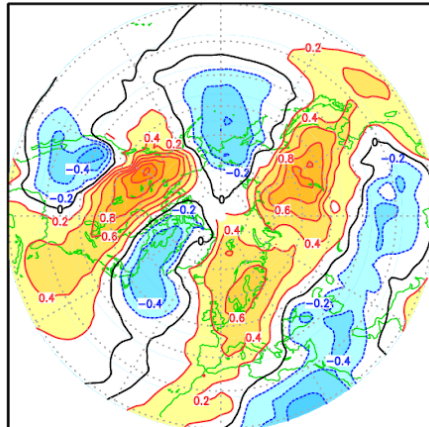
While evidence of the impact of atmospheric resolution and ocean coupling has been limited, this study has highlighted common differences in model performance when teleconnections from different sources and periods are considered. In addition, the analysis of the multi-decadal CERA20C record has confirmed that teleconnections active at interannual time scale also play a major role on multi-decadal scale. Historical ensembles of at least 5 to 10 members for each model configuration would be needed to improve the statistical significance of these results and allow a meaningful (rather than tentative) analysis of the impact of tropical teleconnections on extra-tropical inter-decadal variability, especially in the Atlantic-European region.

A detailed description of the study has been submitted to Climate Dynamics (Molteni et al. 2019).

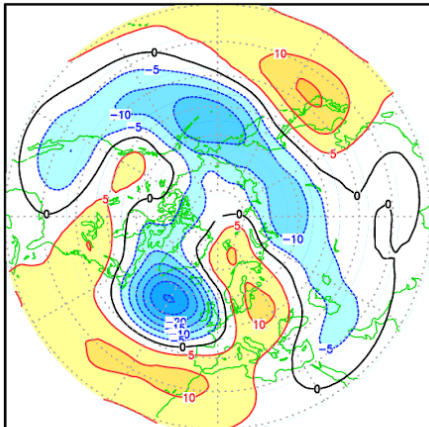
cov [prec(wcio), gh500] cera20cr
dec(2m) 1950 2009



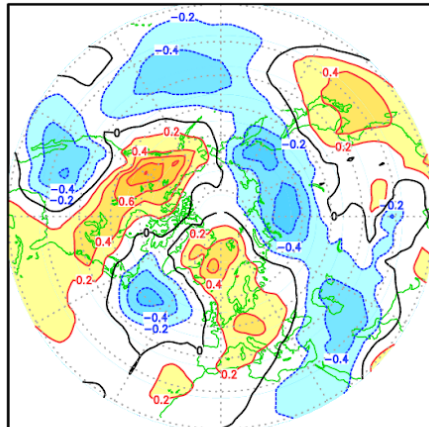
cov [prec(wcio), ta850] cera20cr
dec(2m) 1950 2009



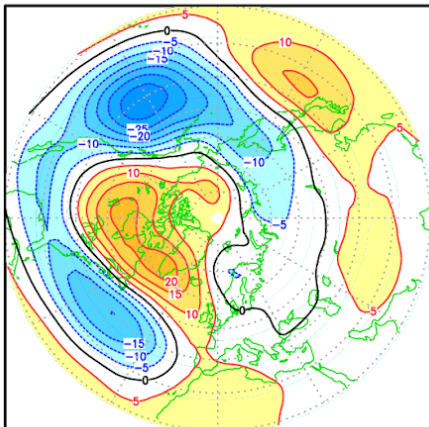
cov [prec(nino4w), gh500] cera20cr
nov(2m) 1950 2009



cov [prec(nino4w), ta850] cera20cr
nov(2m) 1950 2009



cov [prec(nino4w), gh500] cera20cr
jan(2m) 1951 2010



cov [prec(nino4w), ta850] cera20cr
jan(2m) 1951 2010

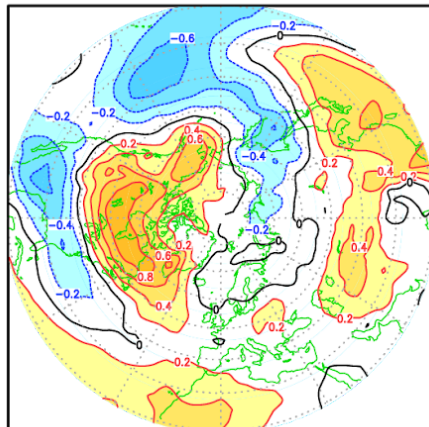


Fig. 3.2.2.1 Left column: covariance of 500-hPa geopotential height over the NH with normalised rainfall anomalies in tropical regions. Top: covariance with western/central Indian Ocean (WCIO) rainfall in Dec-Jan; centre: covariance with NINO4 rainfall in Nov-Dec; bottom: covariance with NINO4 rainfall in Jan-Feb. Right column: as in left column but for covariances with 850-hPa temperature. Data from CERA20C in winters 1950/51 to 2009/10.

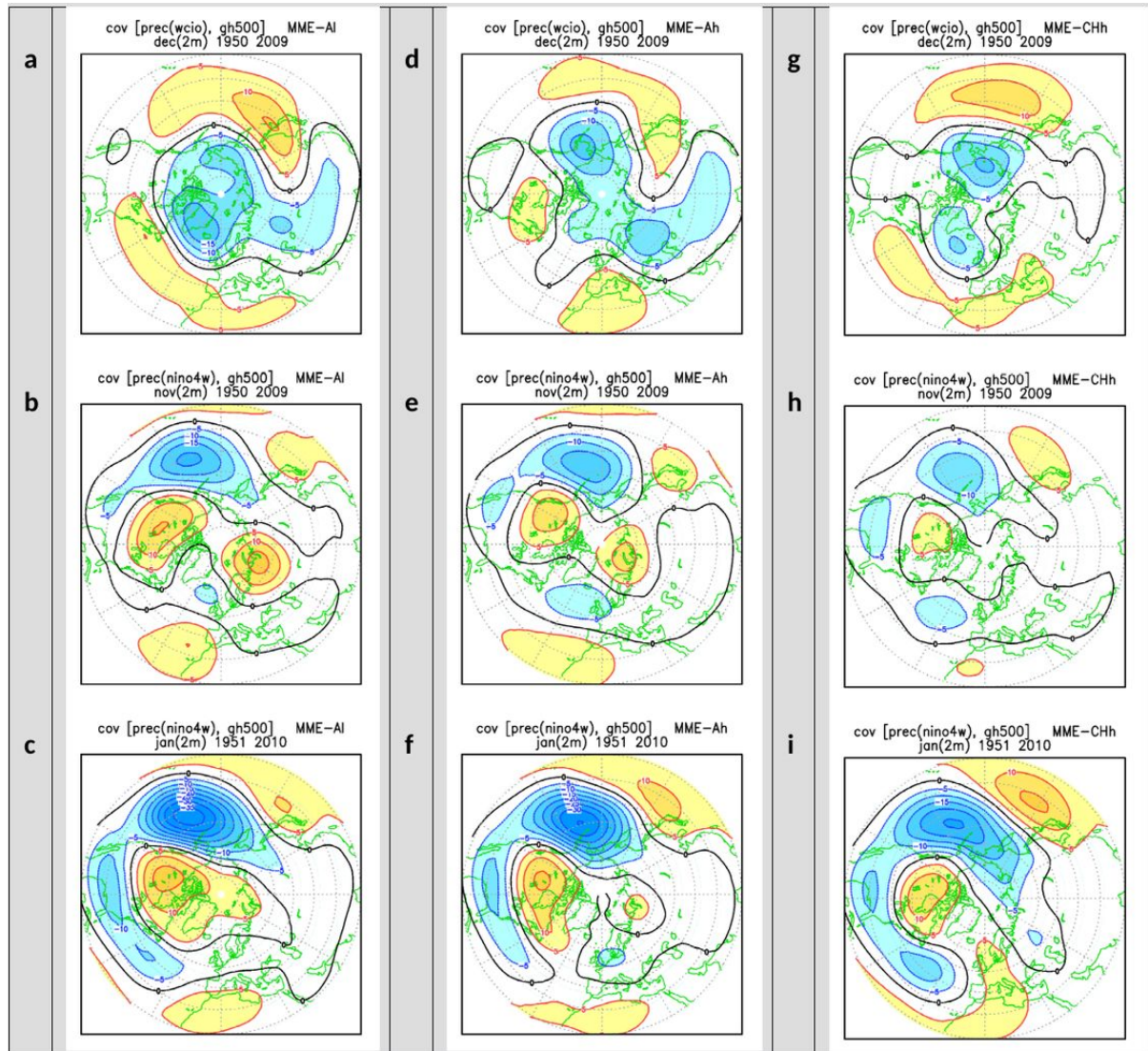


Fig. 3.2.2.2 Teleconnection patterns (as in Fig. 3.2.2.1, left column) computed from the multi-model historical ensembles including single integrations from 6 climate models from PRIMAVERA partners. Left column: low-resolution AMIP ensemble; middle column: high-resolution AMIP ensemble; right column: high-resolution coupled ensemble. Top row: covariance with western/central Indian Ocean (WCIO) rainfall in Dec-Jan; middle row: covariance with NINO4 rainfall in Nov-Dec; bottom row: covariance with NINO4 rainfall in Jan-Feb.

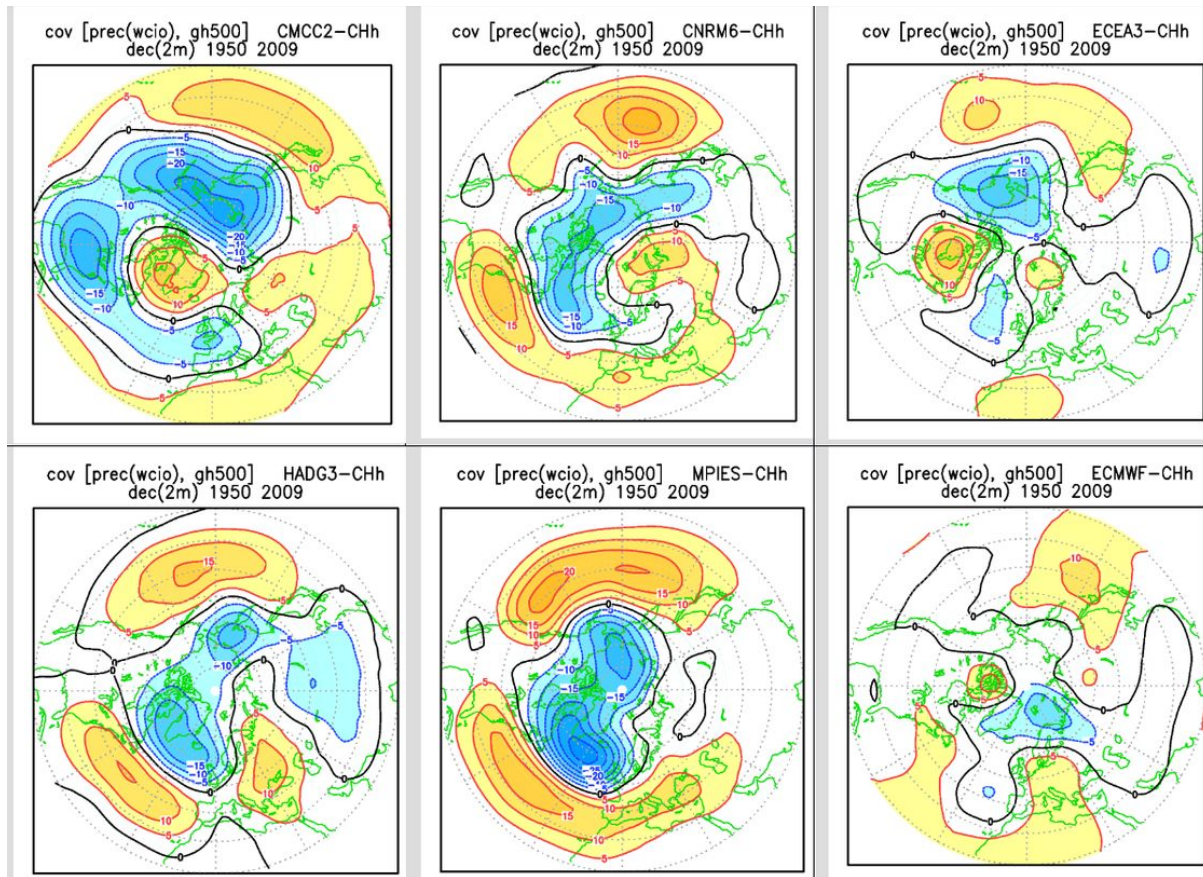


Fig. 3.2.2.3 Teleconnection of WCIO rainfall with 500-hPa height in Dec-Jan in the high-resolution coupled simulations from the six climate models considered in this study.

3.2.3 ENSO influence on Tropical North Atlantic SSTs (CERFACS)

Although the influence of ENSO on the Tropical North Atlantic (TNA) SSTs in boreal spring is one of the most robust ENSO teleconnections and a variety of mechanisms have been proposed to sustain it (Enfield and Mayer 1997, Wang 2005, Chang et al. 2006, Lee et al. 2008, Garcia-Serrano et al. 2017), many aspects of the teleconnection still remain poorly understood. Here, this ENSO-TNA SST link is studied from a multimodel analysis of the PRIMAVERA 1950-control experiments. In particular, 12 models have been analyzed, being 6 of them considered as Low Resolution models (LR) and other 6 as High Resolution models (HR).

A common result from LR and HR models is the fact that the ENSO-related weakening of the trade winds taking place in February (after the peak of the ENSO event) over the study area seems to be crucial for the development of the related response on TNA SSTs, in particular (Figure 3.2.3.3, left & central panels). This result is coherent with recent analyses in the study region (Oettli et al. 2016). However, we found out that this *cause and effect* link between the anomalous surface winds in February and the resultant SST response appears reinforced in HR models (Figure 3.2.3.3; right panels). The underlying explanation is still

under study but it might be related to the representation of the background state of the Atlantic ocean in the models being analyzed. In HR models the mixed layer depth is systematically thinner than in LR models. As a consequence, the coupling between surface winds and SSTs is enhanced and hence the sensitivity of the TNA SSTs to the ENSO-related anomalous winds. This finding also appear to have an influence on the *signal-to-noise* ratio (ENSO-related signal on TNA SSTs vs internal variability of TNA SSTs), which is found noticeably higher in HR models than in LR models.

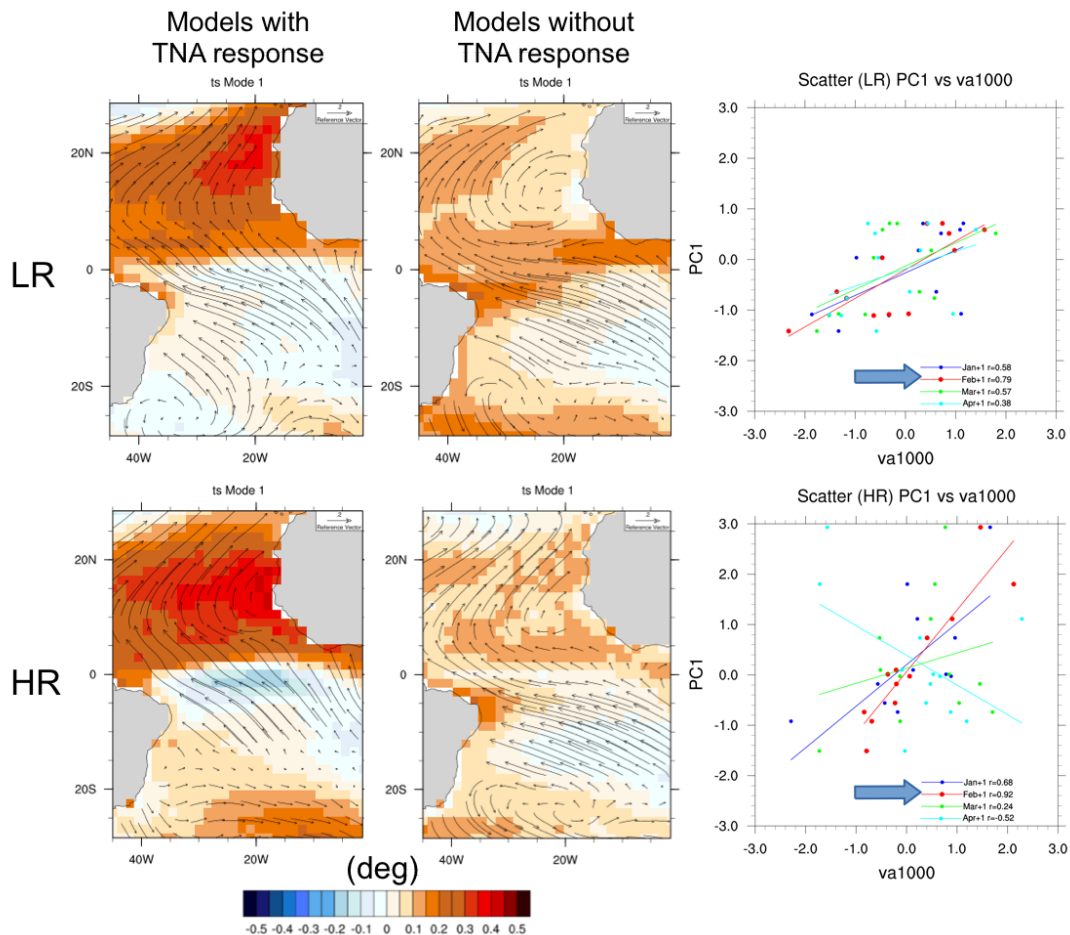


Figure 3.2.3.1 From left to right: 1) the regression maps of those models which capture the TNA SST response to ENSO, 2) the regression maps of those models which do not capture the TNA SST response to ENSO, and 3) the relationship between the surface winds at different months and the SST response. In the top panels the results for the LR models and in the bottom panels for the HR models.

3.2.4 ENSO impact on the Pacific-North American weather regimes (CNR)

The Niño 3.4 index was computed for all the models/ensemble members of the hist-1950 runs. It is based on the SST anomalies averaged across 170°W - 120°W and 5°S - 5°N . The index was computed as the mean anomaly in the above-mentioned area with respect to the climatology in the period 1950-1979 in the same area (Trenberth et al., 2019a). Then, a

5-year running mean was applied and the result was normalized dividing by its standard deviation over the climatological period (1950-1979).

For the PNA sector, the regimes are: Pacific Trough (PT), PNA+, PNA-, Alaskan Ridge (AR). The WRs were calculated for all models and ensemble members of the hist-1950 runs, considering the period 1957-2014 (as for the EAT regimes).

Positive vs negative ENSO

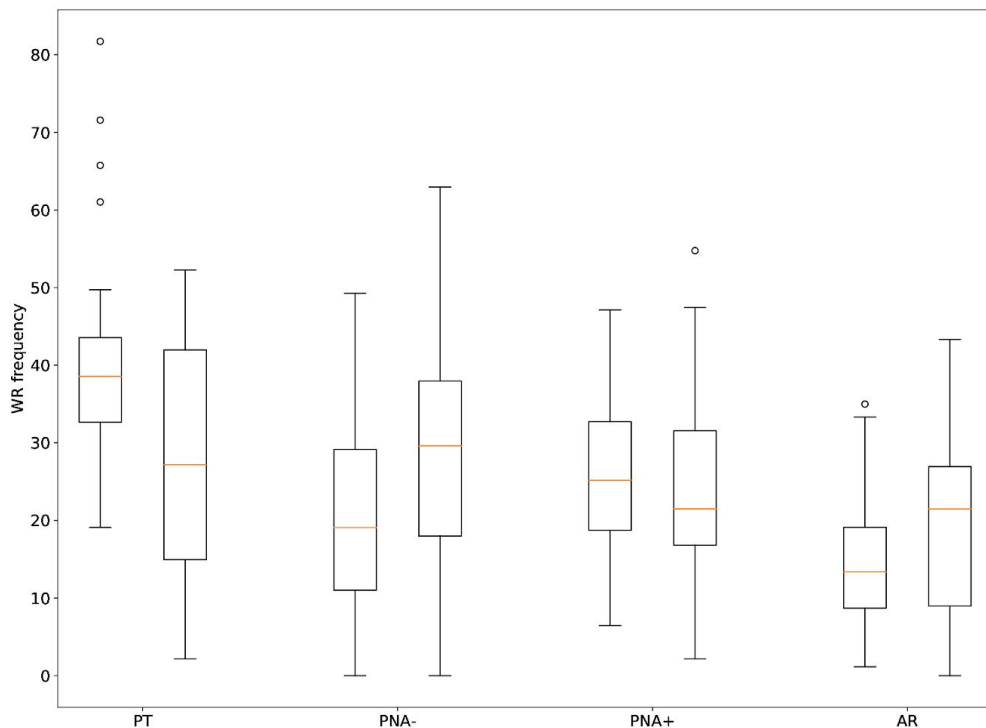


Figure 3.2.4.1 Frequency of occurrence of the PNA regimes with positive (left bar) and negative (right bar) phases of the ENSO (as the ENSO 3.4 Index) for the ERA (40 + Interim) reanalysis (1957-2014). EXPLAIN Box and error bars.

Figure 3.2.4.1 shows the PNA weather regime frequencies distinguishing between seasons with positive and negative ENSO phases, respectively. It can be seen how the PT regime occurrence is higher during positive ENSO seasons, whereas the PNA- and AR have higher occurrences during negative ENSO in winter. PNA+ frequency exhibits no significant changes. These results are in agreement with those by Weisheimer et al (2014).

WR freq. difference between positive and negative phase of ENSO - DJF

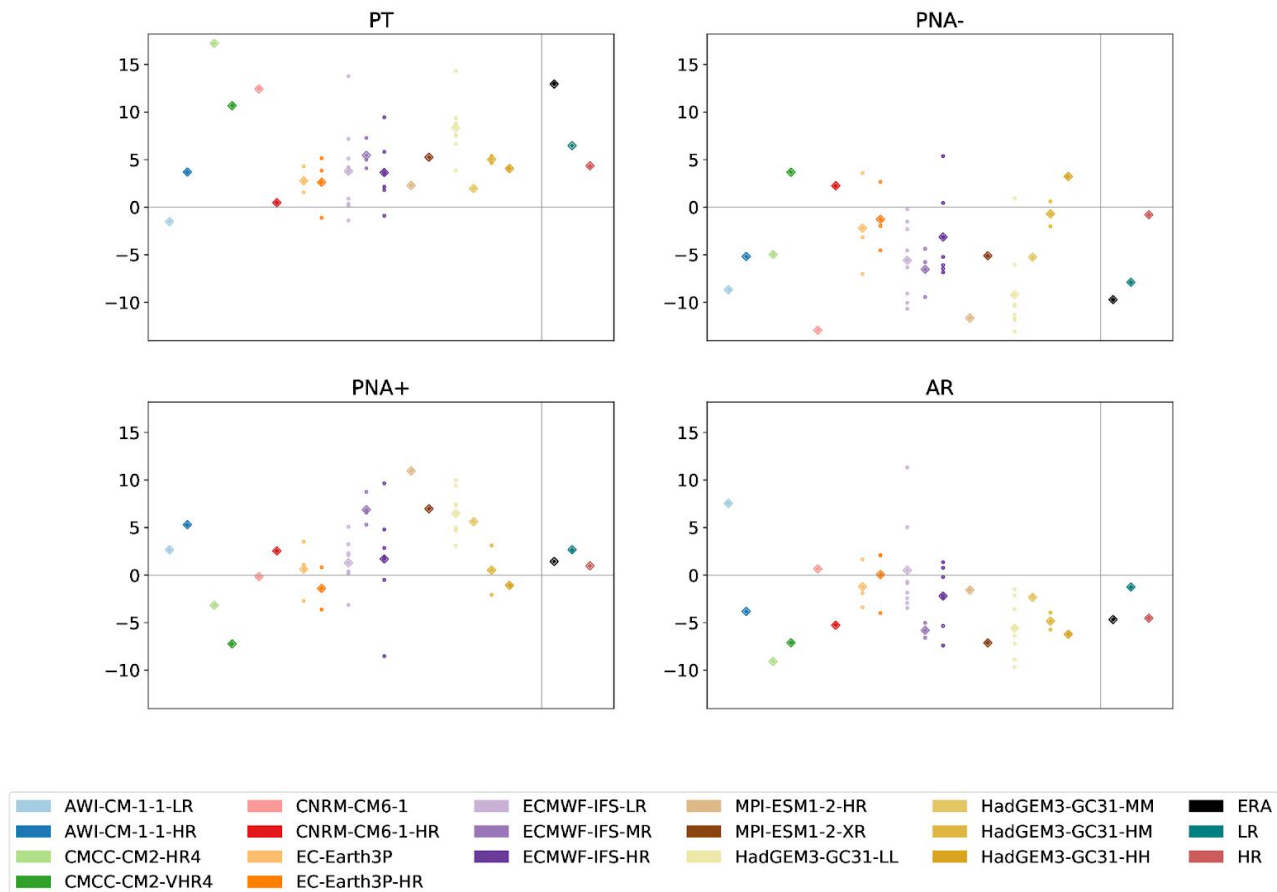


Figure 3.2.4.2 Difference in the weather regime frequencies between positive ENSO seasons minus negative ENSO seasons for all models/members in the hist-1950 ensemble. The diamonds show the model average, the dots the individual members. To the right of the vertical line, the observed value and the average of all lowest (LR) and highest (HR) model versions are shown.

We analysed the link between WR frequencies and ENSO in all primavera models. Figure 2 shows the difference in the WR frequencies computed as the WR frequencies during positive ENSO seasons minus the frequencies during negative ENSO seasons. Whenever a significant correlation between a weather regime and ENSO exists (PT, PNA-, AR), the majority of the models are able to represent such teleconnection as it was observed in reanalysis data. In this case, it seems that the increased resolution does not cause a systematic improvement on how the model capture this teleconnection. A large ensemble spread is found for the PNA+ regime, where also in reanalysis its correlation with ENSO was very weak.

Finally, we investigated the relation between the occurrence of the PT regime and the respective geopotential height anomaly and sea surface temperatures (SSTs) anomalies

patterns. The covariance between the PT frequency and the SST anomalies in the reanalysis shows high covariance values especially over the ENSO region, as expected since the PT is positively correlated with ENSO+ events. The upper tropospheric divergent outflow due to enhanced convection over the equatorial Pacific during El Niño events, in fact acts as a Rossby wave source (see Trenberth et al., 1998 and references therein). This results in a quasi-stationary wave train originating from the tropical Pacific region propagating towards NE into the extratropics of the Northern hemisphere along a great circle, until reaching North America and eventually the Atlantic Ocean. This pattern is clearly visible in the covariance between the PT frequency and the geopotential height anomaly, with the PT being a phase of such stationary Rossby wave train. A ridge is located downstream of the PT over the North American continent with the maximum of geopotential height anomalies located over Canada. Such positive anomaly extends further to the east across the North Atlantic until reaching Europe, resembling a positive NAO pattern. Other regions of positive covariance with the SSTs are the North Atlantic, the Indian Ocean and the South East pacific.

We repeated the same analysis discussed in the previous paragraph to some of the PRIMAVERA models, in particular distinguishing between LR and HR runs. In the ECMWF model a positive covariance between the PT frequency and positive SST anomalies over the equatorial pacific is present but appears much weaker than in reanalysis data. The CMCC model on the other hand shows higher covariance values between the PT frequency and SST anomalies over this region. The MPI model instead fails to represent this teleconnection. In all models apart from the CMCC-VHR run the positive covariance values found over the indian and West Pacific oceans appear missing. Regarding the covariance between the PT frequency and the geopotential height anomaly all models are able to capture the large scale patterns over the PNA area, but the extension of the ridge across the North Atlantic and Europe is much less evident (ECMWF, CMCC) or not present at all (MPI). In all models the increased resolution does not seem to have a relevant impact on this teleconnection.

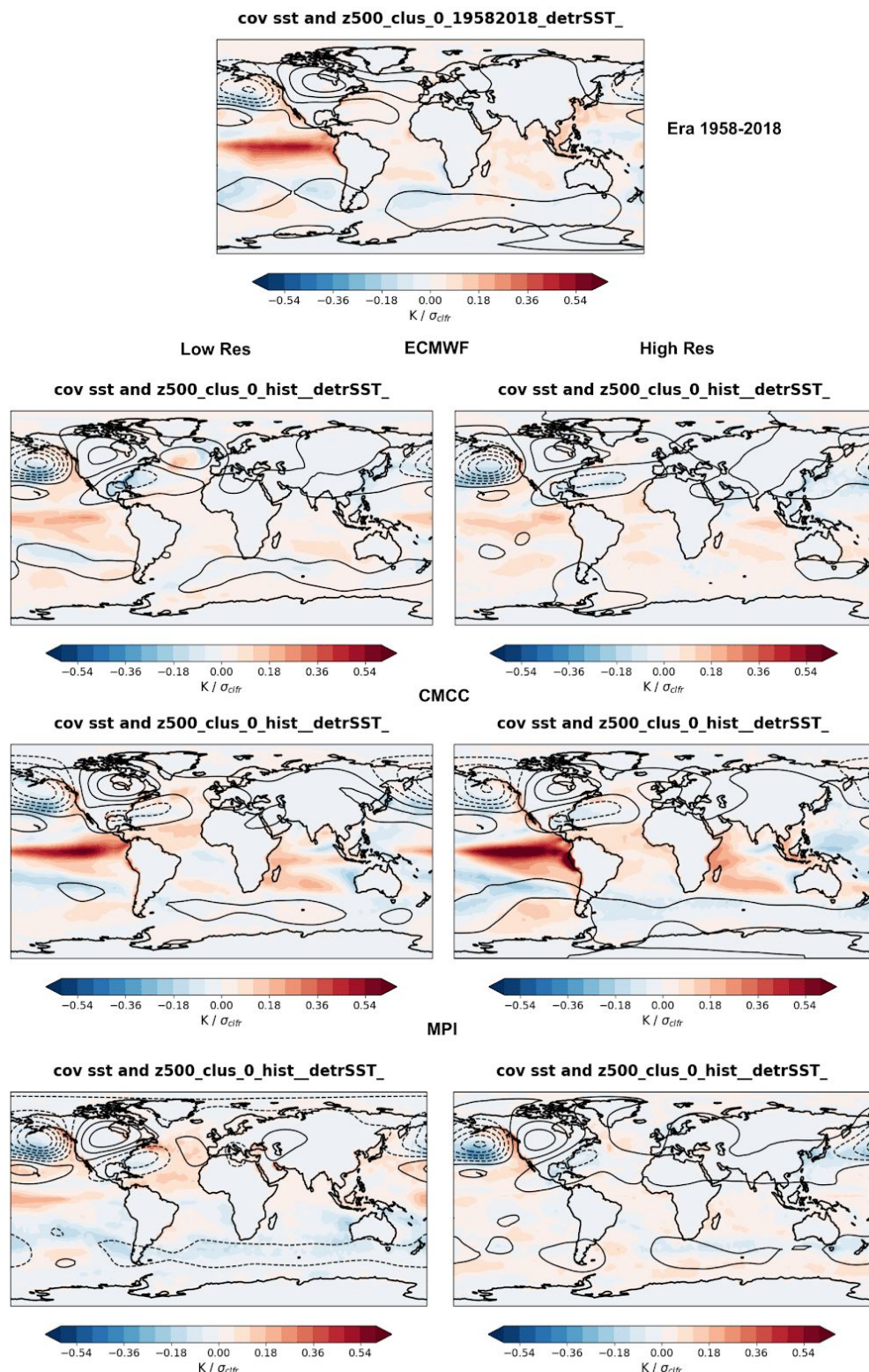


Figure 3.2.4.3 Covariance between frequency of the Pacific trough regime and geopotential height anomaly at 500 hPa (contours every 10 m, dashed lines are negative values) and sea surface temperature anomalies (in colours) for DJF. All values are normalized by the standard deviation of the frequency. Top panel: Era reanalysis (1958-2018). Left column: low resolution simulation for the historical run. Right columns: high resolution historical run.

3.3 Sea Ice

3.3.1 Impact of Arctic sea ice decline on the NH mid-latitudes climate (CERFACS)

This result comes from the PRIMAVERA-WP5 “albedo” coordinated experiments made with the CNRM-CM6.1 model. In these experiments the sea albedo of 40 2-years long members (initialized from the PRIMAVERA 1950-control experiment), is reduced to the ocean values. The resultant sea ice albedo leads to: 1) the same percentage of sea ice loss in LR/HR experiments and 2) a consistent atmospheric responses in LR/HR experiments (Fig. 3.3.1.1, left panels). However, a stronger response in the stratosphere is detected for HR, which translates to a weaker jet stream on its poleward flank (Fig. 3.3.1.1, right panels).

The atmospheric response changes if the number of members increases. In particular, increasing the members decreases the intensity of central Asia cooling in LR and HR experiments and increases the intensity of Europe warming in LR experiments (Figure 3.3.1.2). However, this result should be interpreted with caution, as the results could depend on the choice of members.

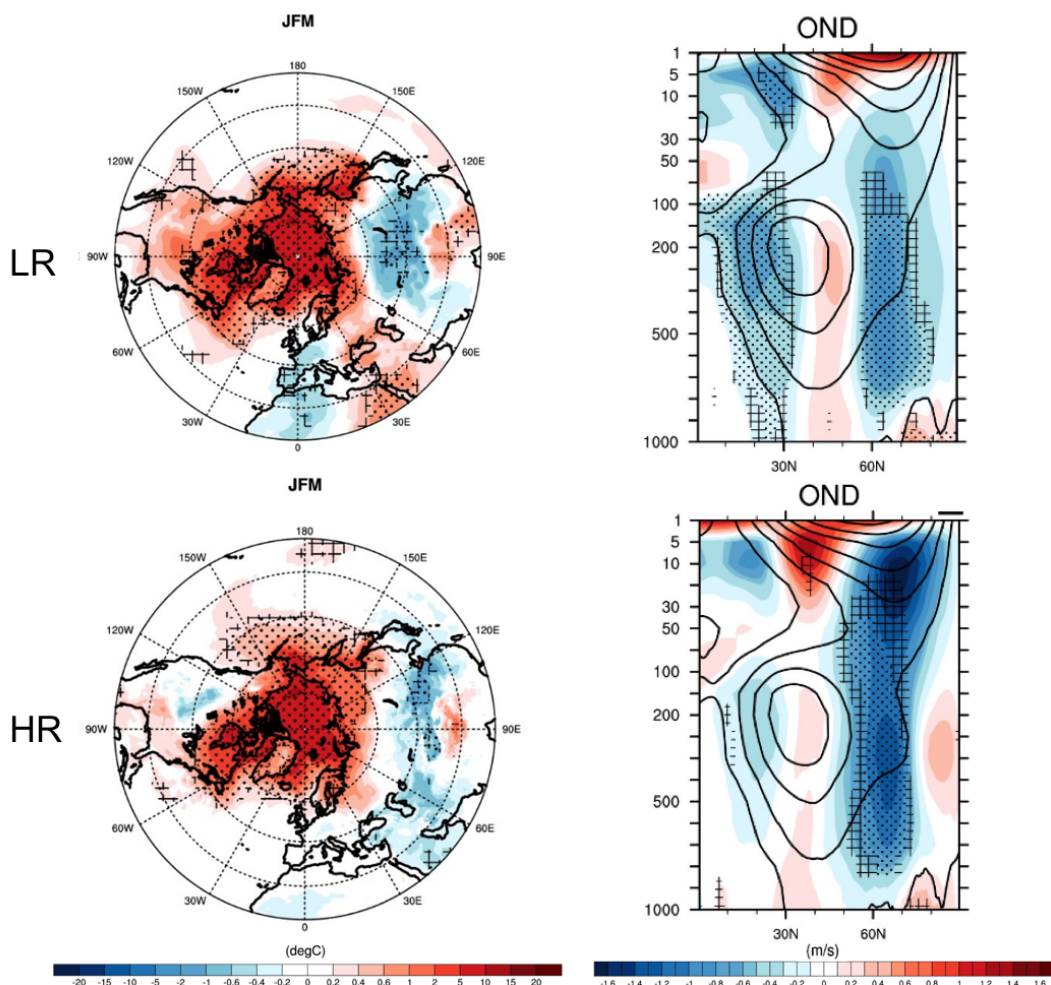


Figure 3.3.1.1 Impact of summer Arctic sea ice decline on: 1) the surface temperature in autumn (left panels) and 2) the zonal-mean zonal wind at different tropospheric and stratospheric levels in winter (right panel). On top, the results for LR and on bottom the results for HR. Dots: significant response at the 5% level (Student's test and FDR approach, Wilks 2016). Crosses: areas where the response is not significant anymore when using the FDR approach.

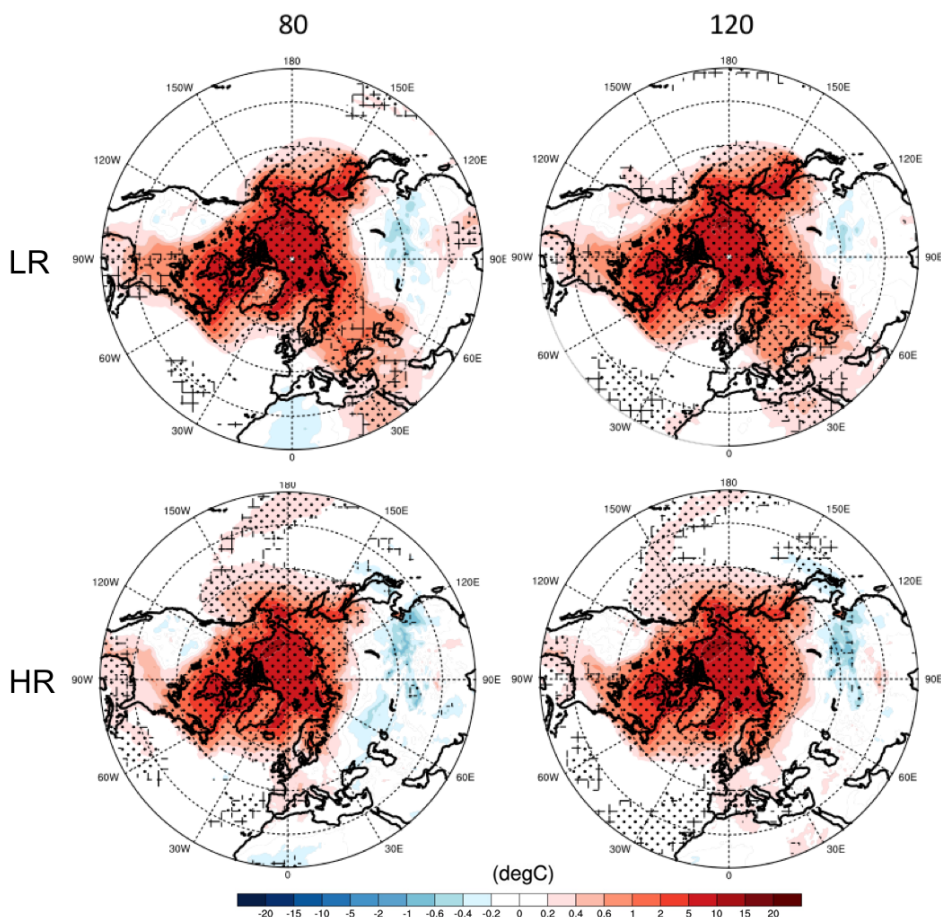


Figure 3.3.1.2 Winter responses of surface temperature in LR and HR experiments, with 80 and 120 members.

3.3.2 Impact of horizontal resolution on the climatic responses due to Arctic sea ice loss (UCLouvain)

The impact of horizontal model resolution on the response of sea ice loss has been analysed at UCLouvain. The results of two coupled models (ECMWF-IFS and CNRM-CM6) run at two horizontal resolutions which performed the PRIMAVERA-WP5 albedo experiments, consisting of 40 members of 15 months long where the sea ice albedo is reduced to the ocean albedo, have been used (Table 3.3.2.1).

	ECMWF-IFS-LR	ECMWF-IFS-HR	CNRM-CM6-LR	CNRM-CM6-HR
Ocean (res)	NEMO 3.4 (~1°)	NEMO 3.4 (~0.25°)	NEMO 3.6 (~1°)	NEMO 3.6 (~0.25°)
Atmosphere (res)	IFS (~50km)	IFS (~25km)	ARPEGE 6 (~1.4°)	ARPEGE 6 (~0.5°)
Sea ice	LIM2	LIM2	GELATO6	GELATO6

Table 3.3.2.1 Components of the two coupled models used.

The sea ice loss caused by the albedo reduction is model and resolution dependent. Indeed, the amount of sea ice loss in these experiments is less pronounced with an increase of the horizontal resolution (Fig 3.3.2.1a). However, the relative loss is more pronounced at high resolution in summer, but less in winter (Fig 3.3.2.1b) for ECMWF-IFS.

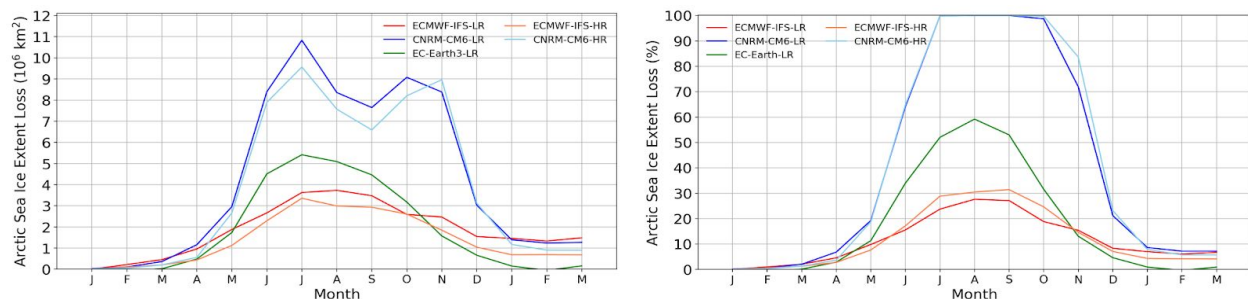


Figure 3.3.2.1 Arctic sea ice extent loss in the 1950-control run and the albedo runs, in absolute value (left) and in relative value (right).

This discrepancy in the sea ice loss can in turn produce different atmospheric responses. In ECMWF-IFS-LR, the sea ice loss extends south of the Labrador sea from December which generates a decrease of sea level pressure over this region in January (Fig 3.3.2.2). By contrast, in ECMWF-IFS-HR, the sea ice loss is mainly restricted in the Davis and Hudson Strait, so the decrease of sea level pressure occurs further west and an increase of sea level pressure is observed over the North Atlantic (Fig 3.3.2.2). This pattern provides other climatic responses over Europe than the low-resolution model in winter, such as colder and dryer anomalies.

In winter, a weakening of the stratospheric polar vortex is detected in ECMWF-IFS-HR, as indicated by the decrease of the zonal wind at 10hPa at 60°N (Fig 3.3.2.3). The weakening of the stratospheric polar vortex is also hinted by an increase of the geopotential height at high latitudes in February (Fig 3.3.2.4). Moreover, a decrease in the tropospheric polar vortex is observed for that month. This leads to a decrease of the geopotential height over midlatitude regions in the troposphere, associated with cooling of the surface temperature over these regions. In the low-resolution ECMWF-IFS-LR, an increase of the geopotential

height is also observed but occurs in March, one month later than at HR. However, this response is not statistically significant and is restricted to the stratosphere only (Fig 3.3.2.4). Therefore, the midlatitude tropospheric circulation response is not affected as in HR and the cooling is very weak.

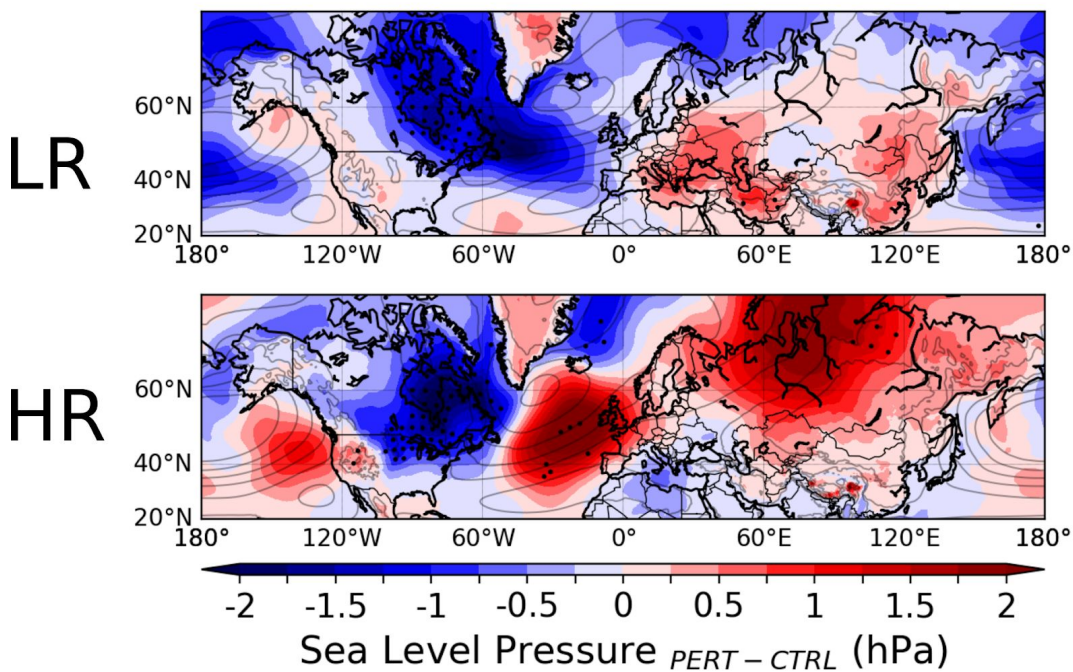


Figure 3.3.2.2 Sea level pressure response in the albedo runs and the control run in winter (JFM) in ECMWF-IFS-LR (top) and in ECMWF-IFS-HR (bottom). Stippling indicates where the response is significant at the 5% level.

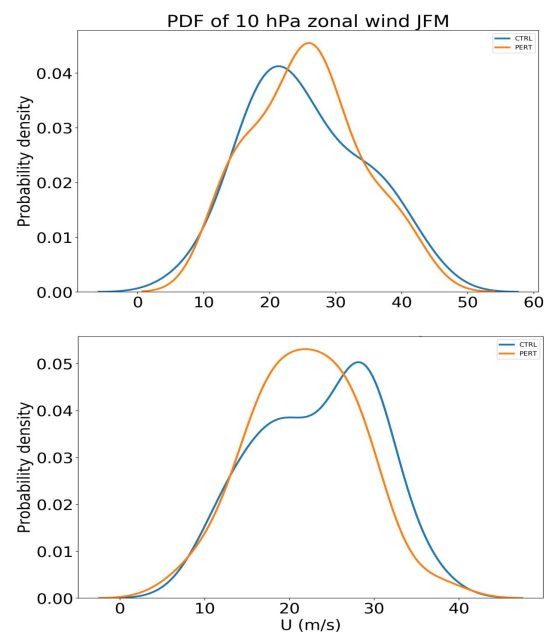
LR


Figure 3.3.2.3 PDF of the zonal wind at 10hPa averaged at 60°N for the control run (blue) and for the albedo runs (orange), for ECMWF-IFS-LR (top) and ECMWF-IFS-HR (bottom).

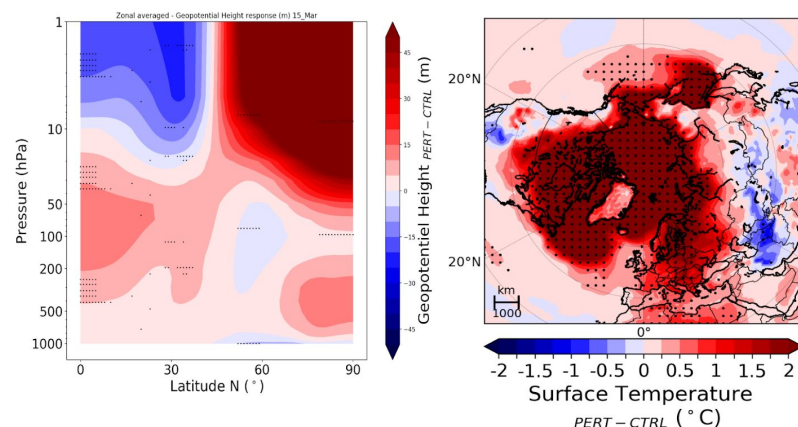
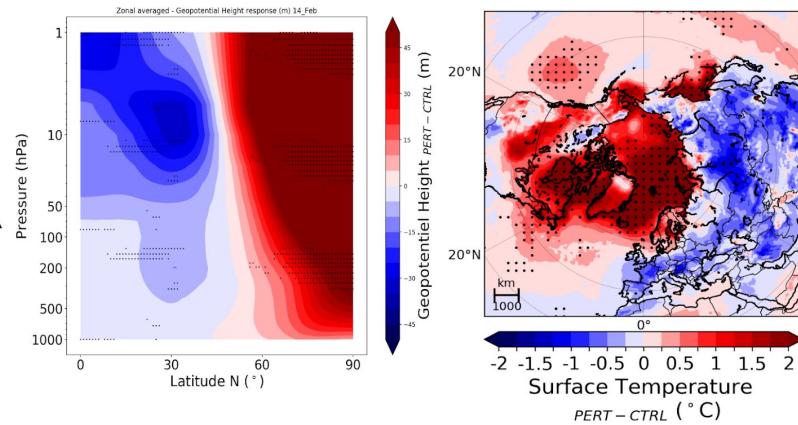
LR

HR


Figure 3.3.2.4 Zonal mean of geopotential height (left) and surface temperature response (right) in the albedo runs and the control run, in March in ECMWF-IFS-LR (top) and in February in ECMWF-IFS-HR (bottom). Stippling indicates where the response is significant at the 5% level.

3.4 Atlantic Meridional Overturning Circulation (AMOC)

The Atlantic Meridional Overturning Circulation (AMOC) transports around 1.2 PW of heat northwards at 26.5°N (Johns et al. 2011) and hence has an important influence on the Atlantic and Arctic climate state and surface fluxes (Docquier et al. 2019; Grist et al. 2018; Jackson et al. 2015). Direct measurement of the AMOC are only available since 2004, hence it is difficult to judge the impact of AMOC interannual variability on Northern Hemisphere climate.

3.4.1 Influence of Atlantic Meridional Overturning Circulation on Northern Hemisphere temperatures (MetOffice)

We have used the control-1950 simulations with constant forcing to look at the interannual relationship between AMOC and surface air temperature. Both timeseries are detrended, and some decades from the initial datasets are excluded to remove model drift. Only one model has been analysed here, HadGEM3-GC31, in order to take advantage of longer simulations completed by this model (compared to the standard 100 years) and because it also includes an eddy-rich ocean model at 1/12° resolution.

Figure 3.4.1.1 shows the regression of the detrended AMOC timeseries, calculated at 26.5°N, against the detrended surface air temperature (TAS), for each model resolution over the number of years shown in each title (using AMOC indices at 40 or 50°N makes little difference to the regressions). It is interesting to note that in the lowest resolution (130km in the atmosphere and 1° in the ocean, henceforth LL) the sign of AMOC and surface temperature is the same over all of the Northern Hemisphere, that is increased AMOC leads to warming over most regions. Over land this warming per Sv of AMOC is up to 0.3K, and considerably more over regions of the ocean. This LL model does have too much sea-ice in the subpolar North Atlantic (Roberts et al. 2019), enhancing the regression here, and in the Arctic the larger regression is a sign of the sea-ice edge receding in years of stronger AMOC. The reduction in sea-ice then leads to a warming over the northern parts of Europe and Russia.

There are some interesting differences at higher resolutions in the atmosphere and ocean. The most notable difference is the change of sign in the regression in the subpolar gyre, over Greenland and parts of North America. Noting that there are fewer years available in most of the higher resolution models, and hence less significance in the patterns, the warming in the Arctic (sea-ice edge retreat) and some signal of this into Northern Europe and Russia is common with LL, while the warming over the North Atlantic Ocean is more restricted to more southerly latitudes.

The importance of these patterns and their differences may become more apparent when trying to attribute changes in surface temperature to processes, be they aspects of variability or perhaps climate change. This work will be extended to more models, and to look at how changes in AMOC over time (including stronger projected future declines at higher resolution, Roberts et al. 2019) may link to changes in temperature over Europe.

Regression of TAS and AMOC@26.5N(detrended)

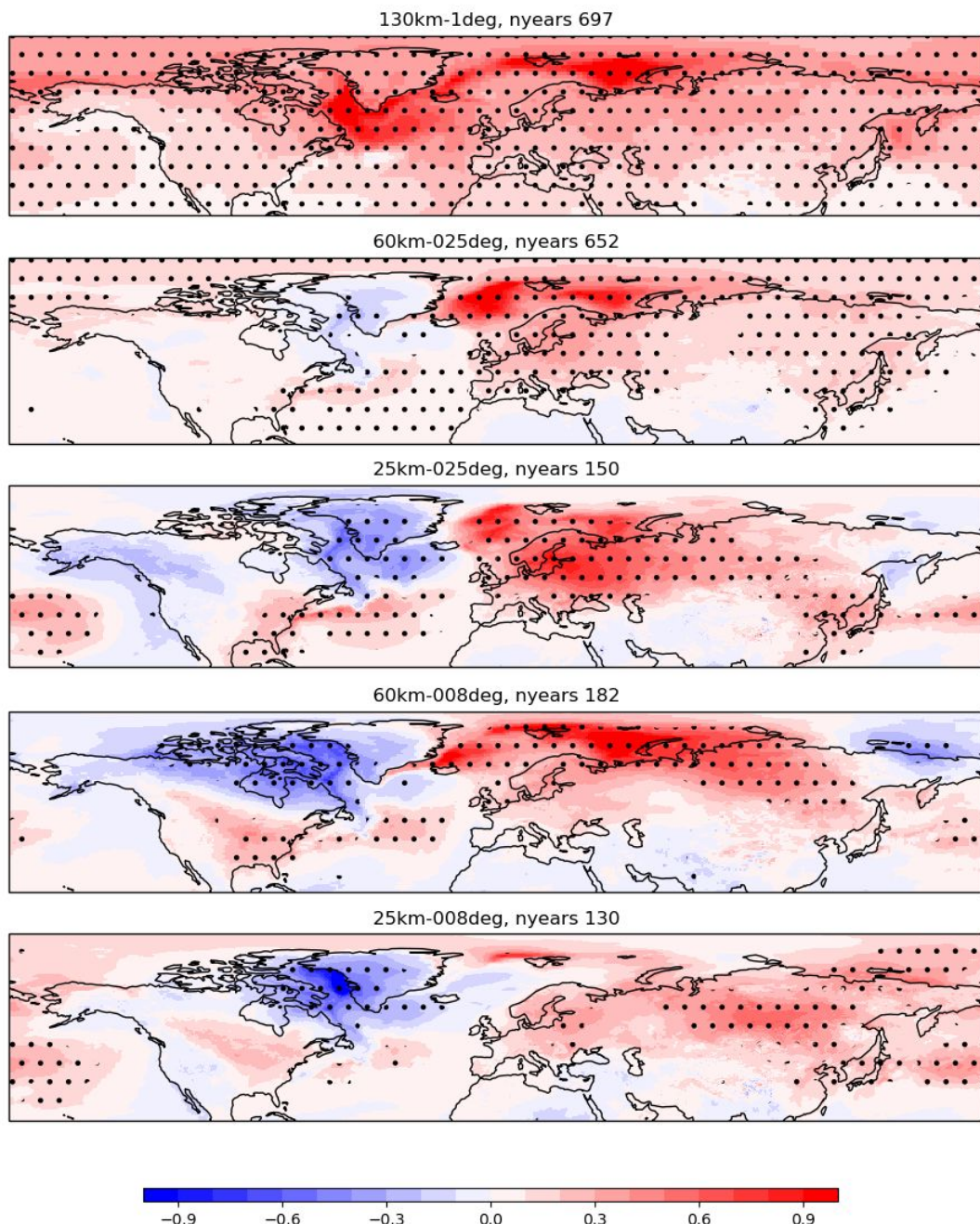


Figure 3.4.1.1 Regression of AMOC timeseries at 26.5°N and annual mean surface air temperature, from HadGEM3-GC31 models at different atmosphere and ocean resolutions. The number of years used is stated in each title. The dots indicate significance at the 95% level. Scale is Kelvin.

3.5 Pacific Decadal Oscillation (PDO)

The Pacific Decadal Oscillation (PDO; Newman et al., 2016) is a large-scale variability mode of the extra-tropical North Pacific and manifests itself with an SST anomaly pattern in the mid-latitude North Pacific, changing polarity with a typical decadal time scale. The corresponding index is defined as the leading principal component of monthly mean SST anomalies in the North Pacific (north of 20°N).

Several studies discuss the possible links between the frontal-scale variability of the Kuroshio Extension (KE) jet and the PDO, through a teleconnection mechanism involving the propagation of baroclinic Rossby waves (e.g. Qiu, 2003; Qiu and Chen, 2005 and 2010).

3.5.1 The influence of the PDO on the Kuroshio Extension low-frequency variability (CMCC)

Here we analyse the impact of model resolution on the interplay between the PDO and the KE low-frequency variability (LFV). The models used are the HighResMIP configurations of the CMCC coupled atmosphere–ocean general circulation model, CMCC-CM2-HR4 (High Resolution, HR) and CMCC-CM2-VHR4 (Very-High Resolution, VHR), which are part of the wider CMCC-CM2 family of models, documented in Cherchi et al. (2018). Both HR and VHR configurations share the same eddy-permitting ocean resolution (ORCA025, i.e. 0.25°). The standard resolution configuration (HR) has an atmospheric resolution of 1° (64 km at 50°N), while the enhanced resolution (VHR) configuration has an atmospheric resolution of 0.25° (18 km at 50°N).

For this analysis we made use of two 100-year present climate simulations conducted using fixed 1950s forcing conditions (referred to as “control-1950” using the HighResMIP terminology). Since the external forcings do not include interannual variability (i.e., no trends associated with observed changes in GHG concentrations, aerosol loadings, ozone and land use are included), only the LFV of intrinsic origin of the coupled system is represented in these control simulations.

The CMCC-CM2-(VHR) models’ ability in reproducing the observed PDO pattern is assessed in Fig. 3.5.1.1. Here, the PDO pattern is diagnosed through the leading EOF of SST anomalies in the [20N-70N] North Pacific domain, following Newman et al. (2016). Both simulated PDO patterns appear to be fairly consistent with observations. The only significant deviation is displayed by HR, featuring a spurious (negative) centre of action off the eastern Japanese coast, which is absent in VHR.

The link between large-scale variability in the extra-tropical North Pacific, as represented by the PDO, and the KE jet is illustrated in Fig. 3.5.1.2, showing the coherence between the PDO phase, the westward propagation of Rossby waves and KE jet length variability (hereafter, LKE). Here, the observed PDO index, SSH anomalies (Hovmöller diagram) and LKE index for the 1993-2017 period are shown. This multi-panel plot is an updated version of Qiu and Chen (2010) and captures a well-established teleconnection between changes in the broad-scale PDO variability mode and the frontal-scale variability of the KE jet, via the westward propagation of baroclinic Rossby waves.

According to this picture, a positive PDO phase, associated with lower (higher) than normal SSH anomalies in the central North Pacific, leads, after propagation across the Pacific Ocean basin, to an increase (decrease) in the KE path length, corresponding to a convoluted (zonally stretched/elongated) state of the KE. These LKE fluctuations are found to be correlated with a meridional shift of the jet (Qiu, 2000), in turn associated with changes in the gyre circulation structure: during the PDO+ (PDO-) phase, the Aleutian Low is stronger (weaker) than normal, the Subtropical Gyre shifts southward (northward) and the negative (positive) SSH anomalies propagate westward, via baroclinic Rossby waves, ultimately affecting the KE variability (e.g. Qiu, 2000; Qiu and Chen; 2005; 2010; Di Lorenzo et al., 2008; Pierini, 2014). Through this mechanism, SSH anomalies generated by PDO fluctuations in the eastern-central Pacific (180-200°E) pace the decadal scale variability of the KE.

Based on this interpretative framework, next we assess whether the same mechanism holds for CMCC-CM2-HR and -VHR models as well. Fig. 3.5.1.3 shows the same diagnostics presented in Fig. 3.5.1.2, but for the two analyzed models. A number of similarities with the observational counterpart emerge, with evidence of PDO-correlated SSH features, travelling westward across the Pacific, getting amplified when reaching the Japan eastern sea-board. In Fig. 3.5.1.4, a zoom on the model years 40-60 time interval is shown, so as to better illustrate the above described chain of events. Figures 3-4 provide clear indications that the pacemaker impact of the PDO on the KE jet variability is well captured in both model configurations.

In order to better characterize the impact of resolution, a more quantitative measure of the PDO-LKE connection is obtained by computing the lagged correlations between the two indices, for HR and VHR. These are shown in Fig. 3.5.1.5, where the PDO leads (lags) the LKE index for positive (negative) time-lags. Note that annual mean values are used for LKE. The correlations between the PDO and LKE show significant correlations for both positive and negative time lags. Focusing on the positive time-lag axis, the large-scale PDO signal appears to lead the frontal-scale LKE index with a delay likely determined by the time needed by a Rossby wave signal to propagate from the central Pacific (PDO center of action) to the KE region. Interestingly, this delay is model-dependent, with HR and VHR reaching their maximum correlations at time-lags 6-8 years and 4 years respectively. The significant correlations found for negative time lags, suggesting an apparent causality between the KE jet and the PDO, requires further investigation.

Summarizing, both models appear to be able to reproduce the mechanism involving the PDO as a pacemaker for the KE LFV, in agreement with previous studies (e.g. Qiu and Chen; 2005; 2010; Pierini, 2014). Increasing the resolution leads to a more realistic PDO representation. However, the oceanic teleconnection mechanism provided by the propagation of baroclinic Rossby waves is well captured in both models, showing little impact associated with the enhanced atmospheric resolution. This might be due to the major role played by the oceanic component in this specific process.

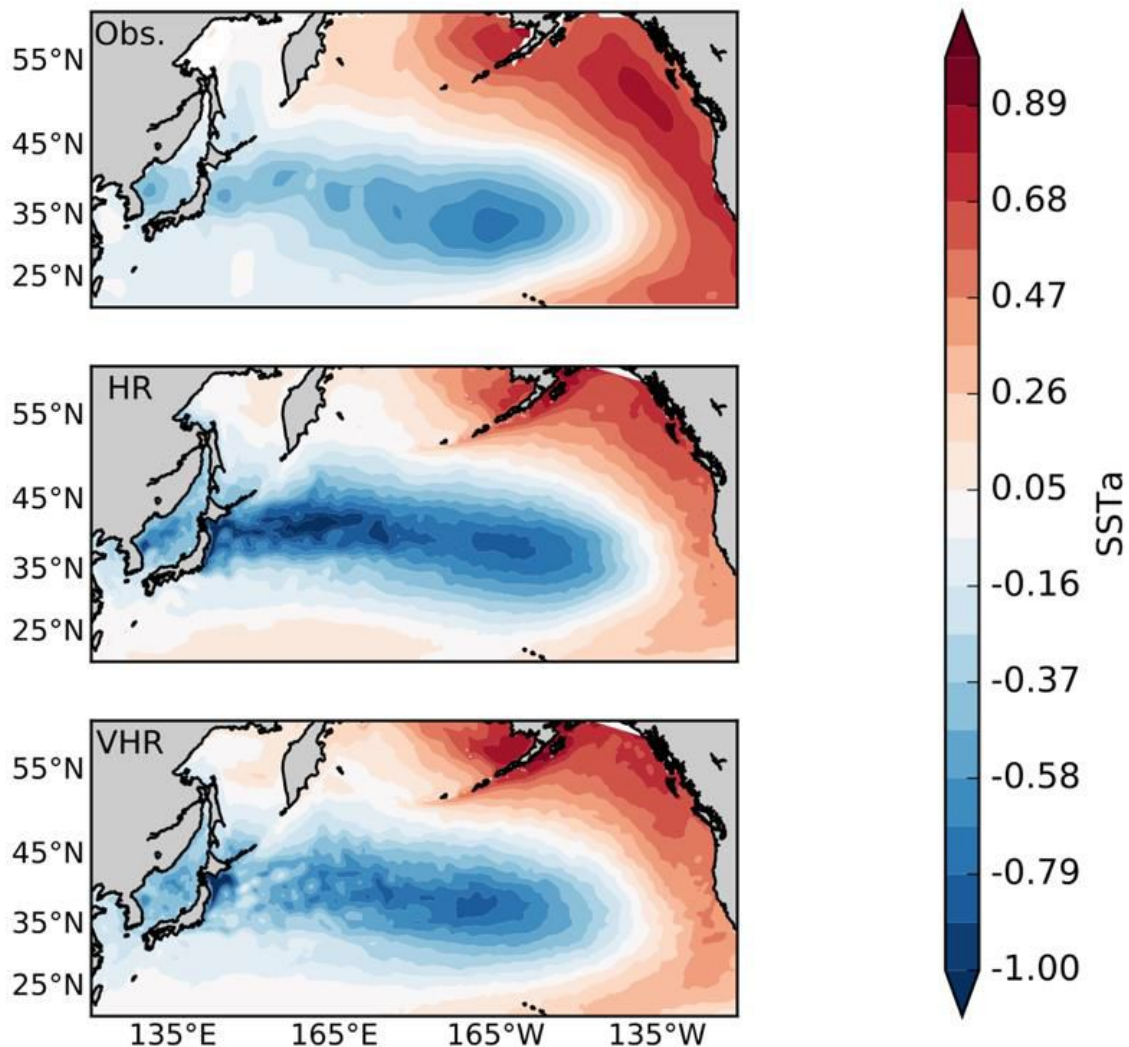


Figure 3.5.1.1 First Empirical Orthogonal Function (EOF) for the SST anomalies field in the North Pacific Ocean in the observations (top), HR (center) and VHR (bottom).

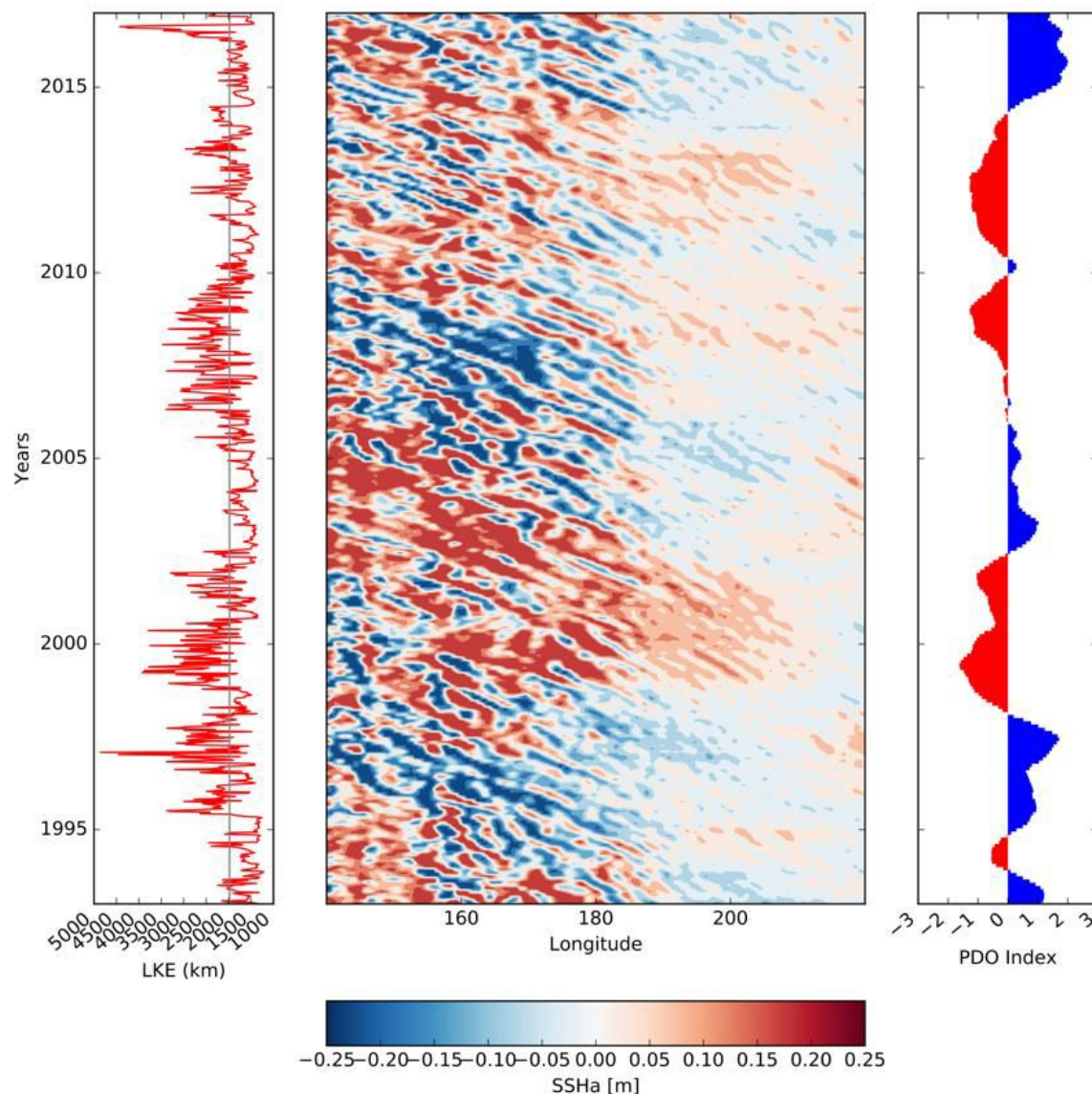


Figure 3.5.1.2 Observational estimates of (left) LKE index (km, shown in red; the long-term mean value is also indicated in grey); (center) Hovmöller diagram of SSH anomalies (m) in the Pacific basin averaged between 32-34°N as in Qiu and Chen (2005); (right) PDO index computed as in Newman et al. (2016).

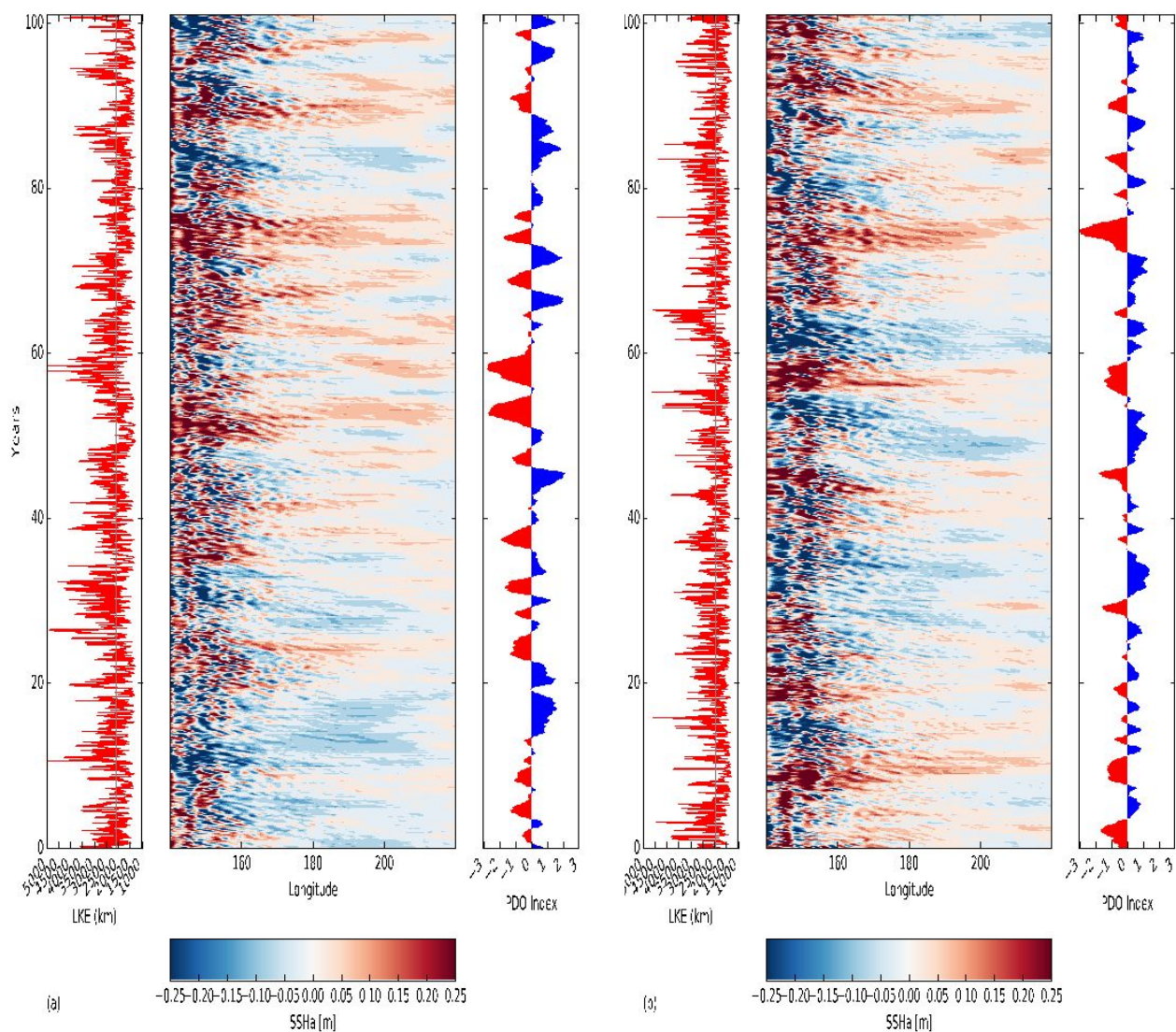


Figure 3.5.1.3 Same as Fig. 2 but for (a) HR and (b) VHR model configuration.

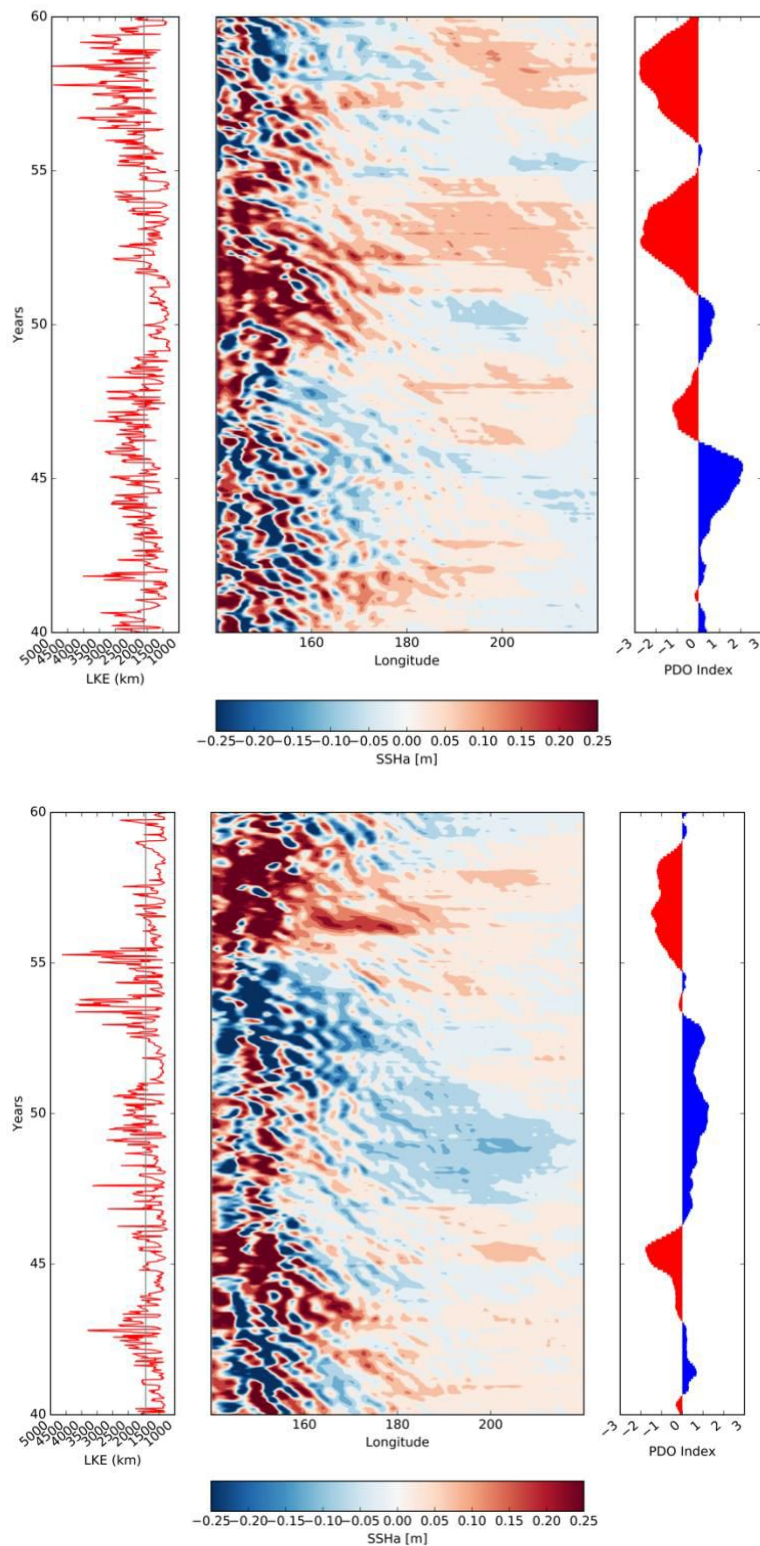


Figure 3.5.1.4 Same as fig.3 but for model years [40-60] interval.

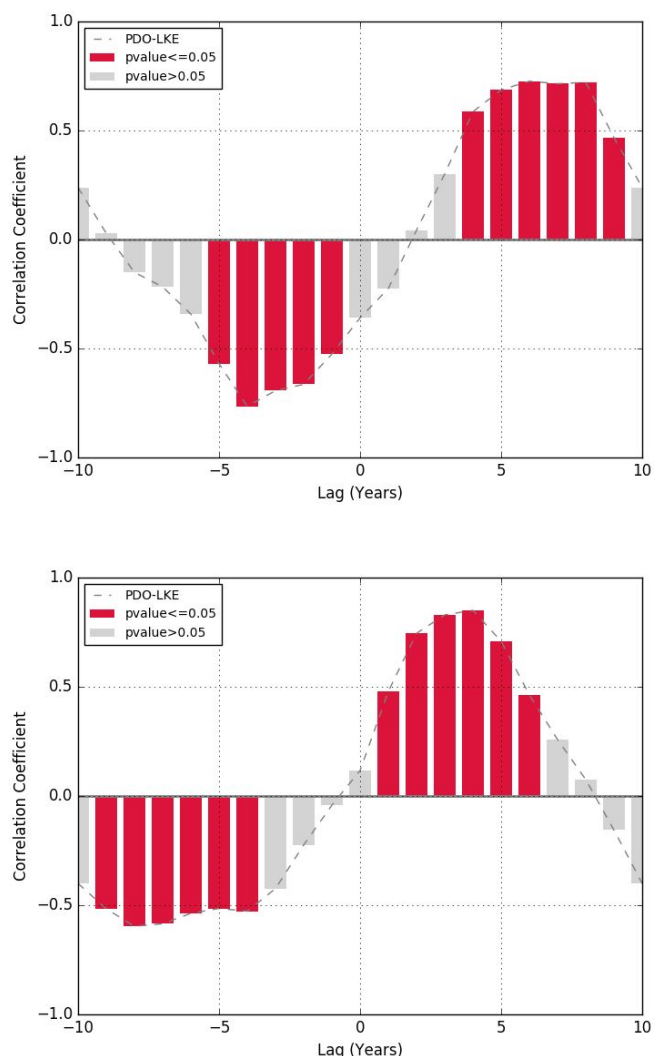


Figure 3.5.1.5 Lead-lag correlation between PDO and LKE in (left) HR and (right) VHR. For positive lags the PDO leads.

4. Lessons Learnt

4.1 Assessment of the model performance in reproducing the observed teleconnections

Many contributions to the deliverable – mainly those focussed on the historical coupled simulations – aim at assessing the model performance in reproducing observed teleconnection mechanisms. Generally, the models have been able to reproduce several observed teleconnections (3.1.1, 3.1.3, 3.2.1, 3.2.2, 3.2.3, 3.2.4, 3.5.1), showing that the physical mechanisms driving these teleconnections are satisfactorily represented in the models (see the Executive Summary section for a quick overview). However, in many cases the multi-model ensemble exhibits a large variability in the amplitude of the associated response, with a general tendency to underestimate it (3.1.1, 3.1.3, 3.2.4). Also, some of the observed teleconnections are much weaker or not reproduced at all by most of the models: this is the case for the AMV impact on Europe surface temperature and geopotential (3.1.1), the WCIO teleconnection to boreal winter circulation (3.2.2), the Pacific Trough regime relation with ENSO SSTs and North-Atlantic geopotential (3.2.4).

Therefore, the general performance of the models in this respect is encouraging, however model biases and the large inter-model variability suggest that some fundamental mechanisms related to the teleconnections are not fully represented by the models. In this sense, additional effort has to be made to improve the representation of the underlying physical processes.

4.2 Impact of the increased resolution on teleconnections

As for many of the processes analyzed here, the models still show noticeable biases with respect to the observations and large differences among them. One of the key questions of WP2 is to assess whether the increased oceanic and/or atmospheric resolutions are playing any role in improving the climate simulations. Many contributions reported no clear impact of the increased horizontal resolution on the model performances (3.1.1, 3.1.3, 3.2.2, 3.2.4, 3.5.1), suggesting that a refined resolution alone is not sufficient to better represent all the observed teleconnections.

Nevertheless, an enhanced horizontal resolution is reported to have a non-negligible impact in some specific cases. Increased resolution may bring the models closer to the observations (3.2.3) or help to enhance the model response to some drivers (3.2.1, 3.1.2). In the case of sea-ice loss (3.3.1, 3.3.2) and AMOC (3.4.1), a detectable impact has been reported but it is difficult to assess whether the increased resolution is bringing the model closer to the real climate. Nonetheless, in the latter case the response of the increased oceanic resolution seems to be more realistic. When other modes of variability are considered, the effect of increasing either the atmospheric or the oceanic resolutions goes in opposite directions (3.2.1) and the overall picture is less clear.

The most interesting cases are those in which the inter-model spread in reproducing a teleconnection have been found to be correlated with biases in the model mean state. This is

the case of the AMV-Pacific teleconnection (3.1.1) and the ENSO-TNA link (3.2.3), where a correlation between weaker teleconnections and a bias in the mean state of the Atlantic ocean has been found. Although no causal link has been provided yet, this suggests that the role of the model mean state beside that of the model resolution may be crucial to better represent the observed teleconnections.

4.3 Potential implications for the future

As concluded in the previous sections, the PRIMAVERA models are generally able to capture the main teleconnection mechanisms, although additional effort is needed to reduce the spread of the model responses. With that in mind, one might ask what we can learn from the present-period results for the future. Given that no future scenario has been analyzed in the context of this deliverable, we can only deduce some future impacts from known expected changes in the large-scale drivers and the teleconnections analyzed here.

From CMIP5 results, the AMV is not expected to change substantially in the future (Villamayor, 2018). If the teleconnection mechanisms analyzed here result unchanged in the future climate, the AMV will continue to be an important source of internal variability for neighbouring (e.g. Europe) and remote regions (e.g. tropical Pacific).

There is no clear result about future changes of ENSO. Some models show an intensification in the short-term projections and a decrease thereafter (Kim et al., 2014), but this result is not robust across all models and the sign of the response is uncertain (Maher et al., 2018). However, ENSO will remain the dominant mode of variability of the climate system (IPCC AR5) and correctly reproducing the ENSO-related teleconnections is fundamental for the representation of future climate. In this respect, the cases of weaker or missing teleconnections in models (WCIO-boreal winter in 3.2.2; AMV-European temperature in 3.1.1) should be further analyzed, given that their poor representations might also affect models' ability to catch the related impacts in future projections.

The results shown in Section 3.3 look at the impact of Arctic sea-ice loss on the boreal winter climate. Since the Arctic sea ice is expected to strongly reduce its extent under global warming, sea-ice loss related impacts are an important component in future climate change. In particular, future sea-ice loss will likely enhance the warming of various polar and subpolar regions (3.3.1) and drive a change in the high latitudes circulation, with a possible weakening of the stratospheric polar vortex (3.3.1, 3.3.2). However, some of these impacts are not completely in agreement between the low and high resolution simulations and deserve additional analysis.

In the context of future changes, very interesting is the result regarding the AMOC teleconnection with the North-Atlantic temperatures and its dependence on ocean resolution (3.4.1). The AMOC is expected to weaken under global warming (e.g. Caesar et al., 2018). A positive correlation between AMOC and surface temperatures in the North Atlantic, as found in the LR HadGEM model, would imply a weaker warming in that region. On the other hand, a negative correlation in the subpolar gyre, as found in the HR models, would increase the warming there, possibly producing another positive feedback on sea-ice. Thus, in order to

reduce the uncertainties for future climate change over the North-Atlantic, it seems crucial to better understand the impact of the AMOC on the surface temperatures.

5. Links Built

This deliverable reports on analyses performed on both WP6 and WP5 sensitivity simulations, thus building a connection between WP2, WP5 and WP6. Regarding the AMV impact on climate, additional and closely related analyses can be found in the dedicated D5.2 deliverable "*Report documenting the impacts of AMV and IPV, and changes in direct radiative forcing, on the European climate of the most recent period and sensitivity to resolution and physics choices*".

The deliverable is also linked to previous WP2 deliverables D2.1, D2.2 and D2.3, regarding the focus on the role of the increased resolution.

References

African environment outlook: Past, present, and future perspectives. United Nations Environmental Program (2002).

Boé, J., F. Habets 2014: Multi-decadal river flow variations in France, Hydrol. Earth Syst. Sci., 18, 691–708, doi: 10.5194/hess-18-691-2014

Boer and co-authors (2016): “ The Decadal Climate Prediction Project (DCPP) contribution to CMIP6”, Geosi. Model Dev., doi: 10.5194/gmd-9-3751-2016

Chang, P., Y. Fang, R. Saravanan, L. Ji, and H. Seidel (2006) The cause of the fragile relationship between the Pacific El Niño and the Atlantic Niño. Nature, 443, 324-328.

Cherchi A, et al., 2018: Global mean climate and main patterns of variabilità in the CMCC-CM2 coupled model. J Adv Model 454 Earth Syst 11:185.

<https://doi.org/10.1029/2018MS001369>.

Dawson A., Palmer T., Corti S. (2012). Simulating regime structures in weather and climate prediction models. Geophysical Research Letters, doi:10.1029/2012GL053284

Di Lorenzo E., Schneider N., Cobb K. M., Chhak, K, Franks P. J. S., Miller A. J., McWilliams J. C., Bograd S. J., Arango H., Curchister E., Powell T. M. and P. Rivere, 2008: North Pacific Gyre Oscillation links ocean climate and ecosystem change. Geophys. Res. Lett., 35, L08607, doi:10.1029/2007GL032838.

Docquier, D., Grist, J. P., Roberts, M. J., Roberts, C. D., Semmler, T., Ponsoni, L., ... Fichefet, T. (2019). Impact of model resolution on Arctic sea ice and North Atlantic Ocean heat transport. *Climate Dynamics*, 53(7), 4989–5017. <https://doi.org/10.1007/s00382-019-04840-y>

Enfield, D. B., and Mayer, D. A. (1997), Tropical Atlantic sea surface temperature variability and its relation to El Niño-Southern Oscillation, *J. Geophys. Res.*, 102(C1), 929– 945, doi:10.1029/96JC03296.

Enfield, D. B., A. M. Mestas-Nuñez, and P. J. Trimble, 2001: The Atlantic multidecadal oscillation and its relation to rainfall and river flows in the continental U.S. *Geophys. Res. Lett.*, 28, 2077, doi:10.1029/2000GL012745.

García-Serrano, J., Cassou, C., Douville, H., Giannini, A., & Doblas-Reyes, F. J. (2017). Revisiting the ENSO teleconnection to the tropical North Atlantic. *Journal of Climate*, 30(17), 6945-6957.

Gastineau, G., and C. Frankignoul, 2012: Cold-season atmospheric response to the natural variability of the Atlantic meridional overturning circulation. *Climate Dyn.*, 39, 37–57, doi:10.1007/s00382-011-1109-y.

Grist, J. P., Josey, S. A., New, A. L., Roberts, M., Koenigk, T., & Iovino, D. (2018). Increasing Atlantic Ocean Heat Transport in the Latest Generation Coupled Ocean-Atmosphere Models: The Role of Air-Sea Interaction. *Journal of Geophysical Research: Oceans*, 123(11), 8624–8637. <https://doi.org/10.1029/2018JC014387>

Häkkinen, S., Rhines, P. B., & Worthen, D. L. (2011). Atmospheric blocking and Atlantic multidecadal ocean variability. *Science*, 334(6056), 655-659

Hannachi A., Straus D., Franzke C., Corti S., Woollings T. (2017). Low-frequency nonlinearity and regime behavior in the Northern Hemisphere extratropical atmosphere, *Rev. Geophys.*, doi:10.1002/2015RG000509

Jackson, L. C., Kahana, R., Graham, T., Ringer, M. A., Woollings, T., Mecking, J. V., & Wood, R. A. (2015). Global and European climate impacts of a slowdown of the AMOC in a high resolution GCM. *Climate Dynamics*, 45(11), 3299–3316.
<https://doi.org/10.1007/s00382-015-2540-2>

Johns, W. E., Baringer, M. O., Beal, L. M., Cunningham, S. A., Kanzow, T., Bryden, H. L., ... Curry, R. (2011). Continuous, Array-Based Estimates of Atlantic Ocean Heat Transport at 26.5°N. *Journal of Climate*, 24(10), 2429–2449. <https://doi.org/10.1175/2010JCLI3997.1>

Laloyaux, P., de Boisseson E., Balmaseda M. et al. (2018). CERA-20C: A coupled reanalysis of the twentieth century. *Journal of Advances in Modeling Earth Systems*, 10, 1172–1195, doi:10.1029/2018MS001273

Lee, S.-K., D. B. Enfield, and C. Wang (2008) Why do some El Niños have no impact on tropical North Atlantic SST?. *Geophys. Res. Lett.*, 35, doi: 10.1029/2008GL034734.

Li, X., S.-P. Xie, S. T. Gille, and C. Yoo, 2015: Atlantic-induced pan-tropical climate change over the past three decades. *Nat. Climate Change*, 6, 275–279, doi:10.1038/nclimate2840.

Mahajan, S., R. Zhang, and T. L. Delworth 2011: Impact of the Atlantic Meridional Overturning Circulation (AMOC) on Arctic Surface Air Temperature and Sea Ice Variability. *J. Clim.*, doi:10.1175/2011JCLI4002.1

McGregor, S., A. Timmermann, M. F. Stuecker, M. H. England, M. Merrifield, F.-F. Jin, and Y. Chikamoto, 2014: Recent Walker circulation strengthening and Pacific cooling amplified by Atlantic warming. *Nat. Climate Change*, 4, 888–892, doi:10.1038/nclimate2330.

Mohino, E., S. Janicot, and J. Bader, 2011: Sahel rainfall and de-cadal to multi-decadal sea surface temperature variability. *Climate Dyn.*, 37, 419–440, doi:10.1007/s00382-010-0867-2.

Molteni F., Roberts C. D., Senan R., Keeley S.P.E. et al. (2019): Boreal-winter teleconnections with tropical Indo-Pacific rainfall in HighResMIP historical simulations from the PRIMAVERA project. Submitted to *Climate Dynamics*.

Newman, M., et al. 2016: The Pacific Decadal Oscillation, Revisited. *J. Climate*, 29, 4399–4427, <https://doi.org/10.1175/JCLI-D-15-0508.1>

Oettli, P., Y. Morioka, T. Yamagata (2016) A Regional Climate Mode Discovered in the North Atlantic: Dakar Niño/Niña. *Scientific reports*, 6, 18782.

Peings, Y., & Magnusdottir, G. (2014). Forcing of the wintertime atmospheric circulation by the multidecadal fluctuations of the North Atlantic ocean. *Environmental Research Letters*, 9(3), 034018

Pierini S., 2006: A Kuroshio Extension System model study: decadal chaotic self-sustained oscillations, *J. Phys. Oceanogr.*, 36, 1605–1625.

Qasmi, S., C. Cassou and J. Boé (2020): “Teleconnection processes linking the intensity of the Atlantic Multidecadal Variability to the climate impacts over Europe in boreal winter”, *J. of Climate*, doi: [10.1175/JCLI-D-19-0428.1](https://doi.org/10.1175/JCLI-D-19-0428.1)

Qiu, B., 2000: Interannual variability of the Kuroshio Extension system 593 and its impact on the wintertime SST field. *J. Phys. Oceanogr.*, 30, 1486–1502.

Qiu, B., 2003: Kuroshio Extension variability and forcing of the Pacific decadal oscillations: Responses and potential feedback. *J. Phys. Oceanogr.*, 33, 2465–2482.

Qiu, B. and Chen, S., 2005: Variability of the Kuroshio Extension jet, recirculation gyre and mesoscale eddies on decadal timescales. *Journal of Physical Oceanography* 35, 2090–2103.

Qiu, B. and S. Chen, 2010: Eddy-mean flow interaction in the decadally-modulating Kuroshio Extension system. *Deep-Sea Res. II*, 57, 1097–1110, doi:10.1016/j.dsr2.2008.11.036.

Roberts, M. J., Baker, A., Blockley, E. W., Calvert, D., Coward, A., Hewitt, H. T., Jackson, L. C., Kuhlbrodt, T., Mathiot, P., Roberts, C. D., Schiemann, R., Seddon, J., Vannière, B., and Vidale, P. L.: Description of the resolution hierarchy of the global coupled HadGEM3-GC3.1

model as used in CMIP6 HighResMIP experiments, Geosci. Model Dev., <https://www.geosci-model-dev.net/12/4999/2019/>, in press, 2019.

Roberts, M.J. and 26 Coauthors, 2019: Sensitivity of the Atlantic Meridional Overturning Circulation to Model Resolution in CMIP6 HighResMIP Simulations and Implications for Future Changes. JAMES, submitted. <https://doi.org/10.1002/essoar.10501560.1>

Ruggieri and co-authors: "Atlantic Multidecadal Variability and North Atlantic Jet: a multi-model view from the Decadal Climate Prediction Project", submitted to J. of Climate.

Ruprich-Robert and co-authors: "Impacts of the Observed Atlantic Multidecadal Variability on Tropical Pacific: a multi-model study", in preparation

Shaman, J., 2014. The seasonal effects of ENSO on European precipitation: Observational analysis. *Journal of Climate*, 27(17), pp.6423-6438.

Schemm, S., Rivière, G., Ciasto, L.M. and Li, C., 2018. Extratropical cyclogenesis changes in connection with tropospheric enso teleconnections to the north atlantic: Role of stationary and transient waves. *Journal of the Atmospheric Sciences*, 75(11), pp.3943-3964.

Straus D. M., Corti S., Molteni F. (2007). Circulation regimes: chaotic variability versus SST-forced predictability. *Journal of Climate*, doi: 10.1775/JCLI4070.1

Sutton, R., and D. L. R. Hodson, 2005: North Atlantic forcing of North American and European summer climate. *Science*, 309, 115–118, doi:10.1126/science.1109496.

Sutton, R., and B. Dong, 2012: Atlantic Ocean influence on a shift in European climate in the 1990s. *Nat. Geosci.*, 5, 788–792, doi:10.1038/ngeo1595.

Tonietto, T. and Scaife, A.A., 2006. The influence of ENSO on winter North Atlantic climate. *Geophysical Research Letters*, 33(24).

Trenberth & coauthors (1998). Progress during TOGA in understanding and modeling global teleconnections associated with tropical sea surface temperatures. *JOURNAL OF GEOPHYSICAL RESEARCH*. doi=10.1.1.453.4672

Trenberth K. & National Center for Atmospheric Research Staff (Eds) (2019ab). Last modified 11 Jan 2019. "The Climate Data Guide: Nino SST Indices (Nino 1+2, 3, 3.4, 4; ONI and TNI)." Retrieved from

<https://climatedataguide.ucar.edu/climate-data/nino-sst-indices-nino-12-3-34-4-oni-and-tni>

Trenberth K., Zhang R. & National Center for Atmospheric Research Staff (Eds) (2019b). Last modified 10 Jan 2019. "The Climate Data Guide: Atlantic Multi-decadal Oscillation (AMO)." Retrieved from

<https://climatedataguide.ucar.edu/climate-data/atlantic-multi-decadal-oscillation-amo>

Vimont, D. J., and J. P. Kossin, 2007: The Atlantic meridional mode and hurricane activity. *Geophys. Res. Lett.*, 34, L07709, doi:10.1029/2007GL029683.

Wang C, (2005) ENSO, Atlantic Climate Variability and the Walker and Hadley Circulations. Revised to the book of the Hadley Circulation: Present, Past and Future, 538 H. F. Diaz and R. S. Bradley, Eds., Cambridge University Press.

Weisheimer A., Corti S., Palmer T, Vitart F. (2014). Addressing model error through atmospheric stochastic physical parametrizations: impact on the coupled ECMWF seasonal forecasting system. Philosophical Transaction of the Royal Society A.
doi:<https://doi.org/10.1098/rsta.2013.0290>